Case Study of a Convective Cluster Over the Rain Shadow Region of Western Ghats Using Multi-platform Observations and WRF Model

Soumya Samanta,[1,2] Kulkarni Gayatri,[1] P. Murugavel,[1] B. Balaji,[1] N. Malap,[1] Y. Jaya Rao,[1]
S. M. Deshpande,[1] S. M. Sonbawne,[1] P. Suneetha,[2] and Thara V. Prabha[1]

Abstract—Unique observational features of a convective cluster, occurred on 12-Sept-2015, over the rain shadow region in the leeward side of Western Ghats have been presented in this study. The synoptic environment had preconditioned the formation of a convergence zone over the study area. Moisture transport from the Arabian Sea was responsible for the moistening in the lower layers. Boundary layer convective thermals contributed to middle level moistening and subsequent onset of the cloud cluster was accompanied by a sudden surge of moist and warm air into the middle troposphere, and subsequent lifting of freezing level (FL) and wet bulb temperature zero (WBT_0) levels. Sudden changes in the FL and WBT_0 levels in association with the gust front prior to the initiation of the cloud system has been documented with high-resolution measurements using microwave radiometer and wind profiler. Thermodynamical parameters from radiometer illustrate the percussive conditions for formation of the cloud system. The cloud cluster had resulted in 25.50 mm rainfall, attributing to $\sim$ 91% of convective rain. Intense fall velocity (10–12 ms^{-1}) was noted up to $\sim$ 7 km during the convective rain and the fall velocity was reduced to $\sim$ 7 ms^{-1} (below the melting layer) during the stratiform counterpart. The cloud system was forecasted using WRF model (version 3.6.1), which was reproduced reasonably well as in the observations and the model output has been analyzed to understand the morphology of the system. The features such as formation of a cold pool, initiation of convective rainfall from the system were well forecasted by the model. Microphysical characteristics of the cloud cluster have also been examined. Riming was the dominant microphysical process within the convective regime. A major contribution to precipitation was from melting of ice hydrometeors especially graupel and snow was noted. Deep warm layer and associated production of supercooled liquid by the lifting of liquid water above the freezing level in updrafts exceeding 15 ms^{-1} was important for the production of a mixed-phase cloud system. Vapor deposition and aggregation process was noted in the stratiform/anvil counterpart, which also contained mixed phase hydrometeors, primarily of snow.

1. Introduction

The Western Ghats (WGs) is one of the most important rain hotspots during the Indian Summer Monsoon (ISM). It serves as a physical barrier to the prevailing south-westerly winds during ISM and receives a copious amount of rainfall (Francis and Gadgil [2006]; Patwardhan and Asnani [2000]; Rao [1976]; Soman and Kumar [1990]; Tawde and Singh [2015]). Numerous studies have been conducted to understand the large scale features, diurnal variation and the cloud characteristics over this rain hotspot. In general, the windward (west) side of WGs receives a huge amount of rain, whereas the rainfall significantly decreases over the leeward (east) side.

Gunnell ([1997]) examined the climatic impact of WGs on ISM and found that the WGs polarizes the precipitation along the crest of the Ghats and on the immediate scarp foot, along with the formation of a secondary offshore convective cloud band. Patwardhan and Asnani ([2000]) analyzed the mesoscale distribution of rainfall during ISM over WGs and identified that the presence of valley modifies airflow thereby controlling the rainfall spatial pattern over this region. Francis and Gadgil ([2006]) found that heavy rainfall events over the west coast of India are mainly associated with the northward propagation of large scale systems (i.e. tropical convergence zone, etc.) and are linked to orography. Using 14 years (1998–2011) of Tropical Rainfall Measuring Mission (TRMM) rainfall dataset, Tawde and Singh ([2015])

[1] Indian Institute of Tropical Meteorology, Dr. Homi Bhabha Road, Pune 411008, India. E-mail: soumya.atmos@gmail.com; soumya.samanta@tropmet.res.in

[2] Department of Meteorology and Oceanography, College of Science and Technology, Andhra University, Visakhapatnam 530003, India.

also found the prominent orographic influence on the spatial variability of rainfall over the WGs region with enhanced precipitation over the windward side and suppressed rainfall over the leeward side.

The westerly jet at a lower level, blowing almost at a right angle to the WGs brings moisture over the Indian landmass during ISM. Analyzing the X-Band radar data over WGs, during the monsoon (June–September) of 2014, Utsav et al. (2017) have also found prominent orographic influence in formation of the clouds over this region. They have reported considerable spatial variability of the storm activity in monthly as well as in the diurnal cycle. The convective cells tend to initiate during mid-night to late morning over the coastal region and at noon to late evening over the leeward side. Clustering of these cells occurs along the mountain ridges. Initiation of convection is found to be more scattered during the night compared to daytime. Most of the cells trigger during afternoon time, which also suggests the influence of diurnal heating along with the orographic lifting. A prominent eastward propagation of convective activity is noted in the diurnal cycle over this region. Maheskumar et al. (2014) have investigated the possible mechanism responsible for high rainfall over the west coast of India. They have argued that the high rainfall over this region is the resultant of the heavy rainfall events along with the continuous medium intensity rainfall. The microphysical characteristics of clouds over WGs have been documented in details by Konwar et al. (2014) with the help of several remote sensing instruments as well as in situ aircraft observations. They have found that in the windward side of WGs, orography induced updraft causes the rapid condensational growth of cloud droplets in shallow precipitation system and helps the formation of bigger droplets which further facilitates collision–coalescence process slightly above the cloud base. During the heavy precipitation events, collision–coalescence process is seen at higher levels and breakup process is dominant at lower levels, whereas during the light precipitation events the raindrops grow bigger in size by the collision–coalescence process during their journey towards the ground.

A nocturnal low-level jet (LLJ) was identified by Prabha et al. (2011) during the pre-monsoon conditions on the eastern slope of the WGs mountain range (rain shadow region) over peninsular Indian region, which is different from the large scale Findlater jet prevailing over this region during monsoon. They reported that the temperature gradient between the valley slope and the adjacent atmosphere is the primary factor for the formation of the nocturnal LLJ among other factors such as slope/valley winds. The moisture transport through these LLJs was also identified in association with atmospheric 'stream' of water vapor in the diurnal cycle. The LLJ over the rain shadow region possesses a strong diurnal variation (Balaji et al. 2017) that has a decisive impact on precipitation processes and its diurnal variation. With the help of high-resolution model simulation, Murthy et al. (2018) have analyzed a hail storm event over the rain shadow region of WGs (over Baramati) and proposed a conceptual mechanism responsible for the event. They have found that outflow from multiple convective cells has helped to organize themselves and trigger new convection in the presence of favorable large scale synoptic features. The outflow from convective clouds has formed a cold pool and associated convergence boundary which interacted with the opposing prevailing wind and formed a zone of wind discontinuity, identified as the potential zone of convective initiation and formation of hail. But the study lacks the observational characteristics of such cloud system as well as its microphysical evolution.

Most of the studies over this region are confined to the windward side of the WGs but little has been explored over the leeward side of the mountain range, especially the detailed observational and simulated characteristics of cloud systems and associated cloud processes. Extensive rain shadow region in the leeward side of WGs frequently encounters severe droughts. Hence, the convection initiation and its life cycle are important for understanding precipitation mechanisms and eventually the diurnal cycle of precipitation. Previous studies lack information about the observed features (using various state of the art instruments) of the cloud characteristics over this region as well as the detailed microphysical evolution associated with the systems, which we have addressed in the present study.

Detailed observational setup was established during the monsoon season of 2015 while Cloud

Aerosol Interaction and Precipitation Enhancement Experiment (CAIPEEX) was underway over the rain shadow region of WGs. The special observational campaign over Pune included wind and thermodynamics observations. One important reason behind the choice of the rain event on 12-Sept-2015 is the availability of several collocated observations (i.e. radiometer, wind profiler along with X-Band radar data). Being the rain shadow region on the leeward side of the WGs less number of rain-bearing systems occur over the study area. The case which has been analyzed in this study, caused a significant amount of rainfall. These are the rare and unique observations of a rain-bearing system over the rain shadow region on the leeward side of WGs mountain range. Apart from this, the system has also been captured well by the model. The motivation behind the present study is threefold: (a) investigating the environmental conditions favouring initiation of the convective cluster, (b) analysis of specific dynamical and microphysical characteristics of the cloud cluster during its lifecycle, (c) how various observations and inferences from high-resolution forecast could be used to have a detailed insight about the cloud system. In this study, an attempt has been made to understand the dynamical, thermodynamical and micro-physical aspects of the cloud system using observations as well as model analysis.

Section 2 provides brief description about different instruments used in this study, the model setup and a brief description of the study area. The synoptic conditions prior to the formation of the system as well as a brief description of the system, various features of the system probed by different instruments, comparison of observed and simulated characteristics and detailed characteristics of the system as forecasted by WRF model have been discussed in Sect. 3. In Sect. 4 we have summarised the results and drawn the conclusion.

2. Data and Methodology

2.1. Instrumentation and Observation

The instruments which have been utilized in this study include Microwave Radiometer Profiler

(MWRP; Radiometrics Inc. model MP-3000A), Wind Profiler Radar (WPR; Astra Microwave Ltd.), X-Band Doppler Weather Radar, Impact Disdrometer (ID), GPS Radiosonde (GPS-RS; Vaisala Inc.) and Automatic Weather Station (AWS). Lightning information from Lightning Location Network (LLN) have been used in this study. ERA-Interim dataset (Dee et al. 2011) have been used to inspect the large-scale condition prior and during the event. INSAT-3D satellite data have been used to examine the large scale evolution of the cloud system and half hourly IMERG dataset (Huffman et al. 2019) is used to examine the spatial distribution of the rainfall associated with the system.

The collocated MWRP, WPR, and ID were installed (Balaji et al. 2017) in the premises of Indian Institute of Tropical Meteorology (IITM), Pune (18.53°N, 73.8°E, AMSL: 560 m). The X-Band radar was located (Utsav et al. 2017) at Mandradev (18.04°N, 73.85°E and AMSL: 1290 m), about 53 km south of Pune. The AWS is situated at Pashan site (18.5°N, 73.9°E) of India Meteorological Department (IMD) and has been used for surface pressure and temperature analysis in this study. The simultaneous observations of various instruments provide useful information about the system and help to explore the state of the atmosphere throughout its lifecycle.

MWRP provides continuous measurements of temperature, vapour density, relative humidity and liquid profile from surface to 10 km in 58 discrete vertical levels. The vertical resolutions of MWRP are 50 m, 100 m and 250 m between the surface to 500 m, 500 m to 2 km and 2 km and 10 km, respectively. The detailed description of MWRP and WPR observations during the observational campaign is given by Balaji et al. (2017). Verification of temperature and humidity profiles against GPS-RS observations have also been conducted in that study. MWRP scans the atmosphere at different predefined angles including zenith and off zenith directions. MWRP recorded temperature and humidity (vapour density) profile at zenith direction have been utilized in the present study and data is available roughly at every 3 min interval. Several stability indices derived from the MWRP data have also been analyzed to

understand the atmospheric conditions prior, during and after the occurrence of the system.

WPR has been used because of its capability to retrieve wind information in all weather conditions. It operates on the principle of scattering of transmitted electromagnetic energy due to the fluctuation of radio refractive index induced by turbulent irregularities. The deployed WPR operates at 1280 MHz and utilizes the Doppler beam-swinging (DBS) technique to measure the height profile of winds (provides reliable data up to $\sim$ 7 km AGL). It provides the zonal, meridional and vertical component of wind vectors. The detail description of WPR is documented by Balaji et al. (2017).

The X-Band Doppler weather radar (frequency 9.535 GHz) was operated in a hybrid scan strategy which included a series of plane position indicator (PPI) sweeps at increasing elevation angle from 0.5° to 90° (in 18 elevation angles) and followed by a range height indicator (RHI) scan. The range of the radar was 125 km, which was very helpful in the study of convective activity over Pune. The radar provided useful information such as reflectivity, radial velocity, spectral width, etc. We have gridded the radar data into Cartesian coordinate using TITAN Software (Dixon and Wiener 1993). In the present study, the constant altitude plan position indicator (CAPPI) at 5 km (AMSL) has been used to understand the evolution and movement of the system as well as to compare the observed radar reflectivity with the WRF simulated reflectivity.

The rainfall observation has been derived from ID, co-located with the MWRP and WPR. It provides the size distribution of raindrops from 0.3 mm to 4.5 mm in 20 bins and the rainfall intensity in every 30 s. The hourly rainfall has been calculated as: for every consecutive 1 h time period, the data at an interval of 30 s have been summed up and the total value has been assigned to the upper limiting hour of the respective period. For example, between 09:00 and 10:00 UTC, the data at an interval of 30 s have been summed up and the total value has been assigned corresponding to 10:00 UTC.

GPS-RS observation was taken as part of special daily flights for CAIPEEX on 12-Sept-2015 at 08:04 UTC at Pune (18.53°N, 73.8°E, AMSL: 560 m). It transmitted the data in each 2-s interval. IITM has

established a dense network of lightning sensors. About 20 sensors from Earth Networks Inc., USA have been used to cover the wide area of Maharashtra, India. These sensors are installed about 150–200 km apart and can detect lightning locations with 90% detection efficiency.

We have also utilized INSAT-3D Thermal Infrared-1 (TIR1) brightness temperature (BT) data, which measures the radiance at 10.8 μm wavelength, to witness the large scale structure of the convective system. The region of BT less than 233 K has been investigated in details as it indicates the deep convective clouds (Arnaud et al. 1992; Mathon and Laurent 2001; Mathon et al. 2002; Goyens et al. 2011). Satellite data is very helpful to monitor the overall evolution of the system.

2.2. Model Description

We have used the Advanced Research WRF (Weather Research and Forecasting) Model (WRF V3.6.1) in forecasting mode to study the evolution of the system. The model is configured with two, two-way nested domain and resolution of the outer and inner domain was 5 km and 1 km, respectively. The lowest level in the model is kept at 25 m above the surface and the model top at 20 km. The model initialization is done by using NCEP GFS (Global Forecast System) data on a 0.25° × 0.25° grid and the outer boundary is updated every 3 h.

The boundary layer parameterization scheme used is Yonsei University (YSU) non-local PBL scheme (Hong et al. 2006) coupled with the Monin–Obukhov (MO) similarity scheme and Noah land surface scheme. The outer domain is parameterized with Kain–Fritsch cumulus parameterization scheme (Kain 2004) and the inner domain is cloud resolving and WRF Double Moment 6 class (WDM6) microphysics scheme (Lim and Hong 2010) is used. The long wave and short wave radiation are parameterized by using Rapid Radiative Transfer Model scheme (Mlawer et al. 1997) and Dudhia scheme (Dudhia 1989), respectively. The land surface scheme is Unified Noah Land Surface Model (Tewari et al. 2004). The static geographical data are taken from the WRF repository as standard datasets. For terrain elevation the 1 km × 1 km (30 s) dataset and

for Land-use data the MODIS derived products are used in this study. Figure 1a shows the outer and inner domain overlaid with NOAA NGDC GLOBE terrain height data. This high resolution (1 km) terrain height information shows the detailed terrain height variability over the study region (NOAA NGDC GLOBE dataset used for illustration purpose).

Simulation is carried out in forecasting mode for the period from 06:00 UTC, 12-Sept-2015 to 06:00 UTC, 13-Sept-2015. Hourly model outputs are analyzed to investigate the evolution of dynamical, macrophysical and microphysical signatures of the system. The first 2 h are considered as the spin-up time for the model, which we have excluded in our analysis.

2.3. Description of the Study Area

We have conducted our study over Pune city (18.53°N, 73.86°E, AMSL: 560 m) which has a population of more than three million and is the 9th most populous city of India (as per Census 2011). Pune is situated nearly 80 km away in the leeward side of the WGs and the city receives on an average 600 mm rainfall during monsoon season (Konwar et al. 2014). WGs run parallel to the west coast of India, in the vicinity of Arabian Sea with an average elevation of 1200 m which is extended nearly

1600 km from north to south. WGs Mountains act as a barrier and block the south-westerly monsoon wind, which causes a copious amount of precipitation over the west side of WGs in monsoon seasons (approximately 10 times more rainfall than that over the eastern side of WGs). Meanwhile, over the eastern side of WGs, the rainfall is considerably reduced. These two factors; WGs as a rain hotspot during monsoon by acting as a barrier and the less prevailing rain over the rain shadow region, makes this a proper test bed to study the monsoon clouds and their efficiency to make rainfall.

3. Results and Discussions

3.1. Synoptic Conditions and Case Overview

Synoptic conditions prior to (Fig. 2a–f) and during (not shown in the figure) the system has been analyzed with the help of ERA-Interim reanalysis data (at a spatial resolution of 0.125°). At 06:00 UTC, warmer (> 35 °C) surface temperature (at 2 m) was observed over the north-western part of India and adjoining regions (Fig. 2a), which further intensified at 12:00 UTC (not shown in the figure). The offshore trough was prevailing at the west coast of the Indian peninsula and is evident through mean sea level
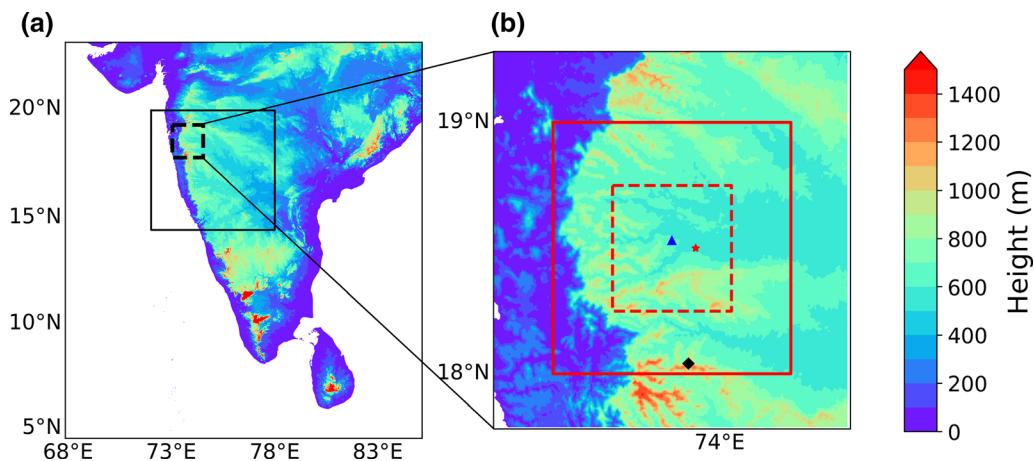

Figure 1

a Terrain height (in m) overlaid with model domain. Inner solid box represents the nested domain. Inner dashed box represents the study area and **b** terrain height (in m) overlaid with enlarged study area. Solid and dashed red box represent the 1° × 1° and 0.5° × 0.5° domain respectively, over which the model output are analysed. Blue triangle shows the location of co-located GPS-RS, MWRP, WPR and ID (IITM premises). Red star shows the location of AWS. Black diamond shows the location of X-Band Radar
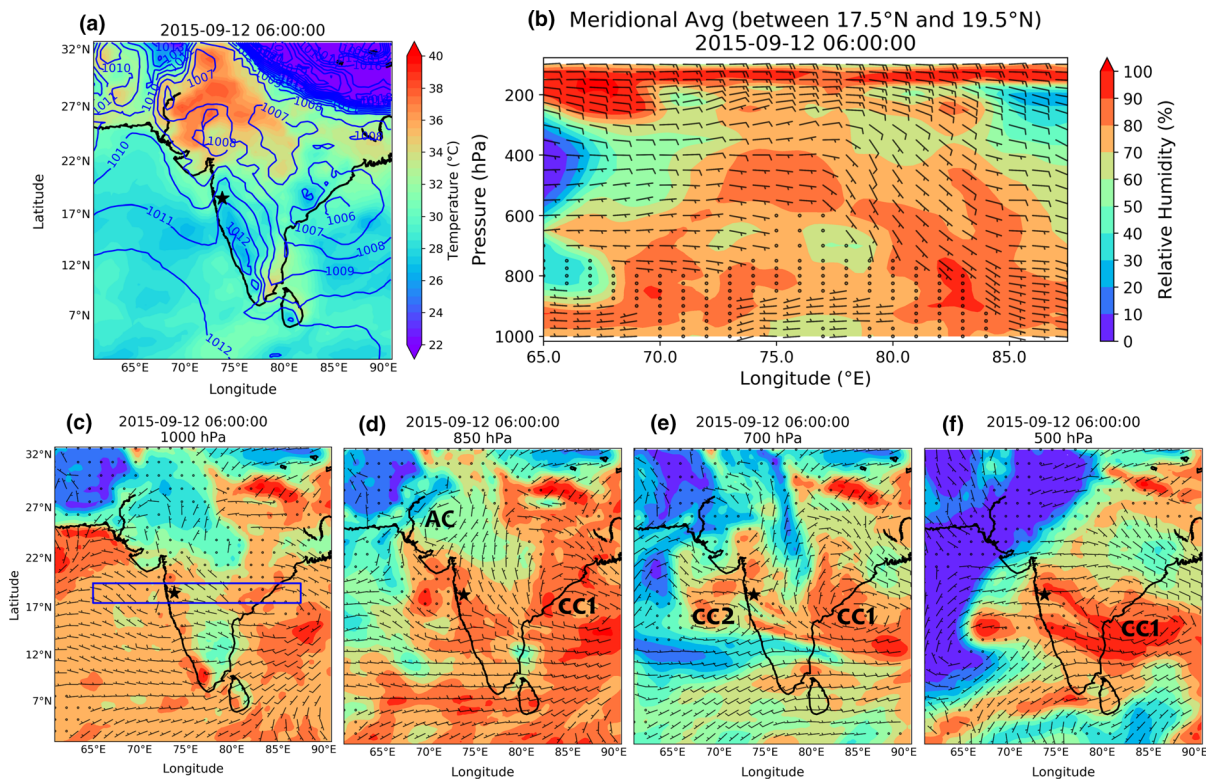
Figure 2

ERA-Interim (resolution: 0.125°) at 06:00 UTC, 12-Sept-2015. **a** Surface temperature (at 2 m) (in color shading) and mean sea level pressure (in hPa) (in blue contours). **b** Longitude vs. height of meridionally averaged (between 17.5°N and 19.5°N) relative humidity (color shading) and wind (standard wind barbs). Spatial distribution of RH (in %) (in color shading) and wind (standard wind barbs) at **c** 1000 hPa, **d** 850 hPa, **e** 700 hPa and **f** 500 hPa pressure level. **b–f** Shares same colorbar. Blue box in **c** indicates the region over which the meridional averaging is done in **b**

pressure (Fig. 2a). The weak westerly wind prevailed at 1000 hPa [Fig. 2c (at 06:00 UTC)] throughout the time (from 00:00 tom 18:00 UTC) over the study region. At 850 hPa, a shallow anticyclonic circulation (high-pressure system) (here after AC) was observed over north-western part of India (over Rajasthan) and adjacent areas and a deep cyclonic circulation (here after CC1) was observed over the north-west Bay of Bengal (BoB) (over Odisha and Andhra Pradesh coast) (Fig. 2d). Though AC weakened with time, the dry northerly outflow from AC over the study region was consistent. A steady and persistent westerly flow near ∼ 15°N latitude can be seen at 850 hPa over the peninsular Indian region. The dry northerly flow at the north of the study area pushed the moist air southward, whereas the steady westerly flow near ∼ 15°N latitude possibly prevented the propagation of the moist air further southward, resulting in pilling up

of moisture over the study location at that level. Another mid-level weak cyclonic circulation (here after CC2) was observed at 700 hPa (but was not well developed at lower levels) off the west coast of the study area (Fig. 2e) and persisted throughout the study period. The south-westerly wind at the southeast sector of CC2 interacted with north-easterly winds and northerly outflow of AC, resulting in a convergence line of moisture over the study region at 700 hPa. Easterly flow over the study region and south-westerly flow in the southern sector can be seen at 500 hPa (Fig. 2f). CC1 was also present at this level. Strong easterlies (∼ 15 to 20 ms^{-1}) prevailed above 500 hPa over the study region (not shown in the figure).

Figure 2b shows the meridional averaged relative humidity and winds over the study area at 06:00 UTC. It provides the average relative humidity and

wind information in 'longitude vs. height' form within the latitudinal belt between 17.5°N and 19.5°N (as indicated with a blue box in Fig. 2c), collocated with observation site (IITM premises) at the latitudinal center. It can be seen that by 06:00 UTC the weak lower level westerlies contributed to some moisture transport (from Arabian Sea) over the WGs, though there was less moisture incursion inland. However, the westerlies strengthened with time and the study region experienced more moisture incursion by the westerlies within the boundary layer (not shown in the figure). The circulation associated with CC1 transported moisture from BoB by the easterly wind and was responsible for moistening near $\sim$ 500 hPa over the study area. The cumulative influence of lower level moisture content, mid-level dry air incursion from the north (at $\sim$ 850 hPa and $\sim$ 700 hPa) and moistening near $\sim$ 500 hPa by the easterly made the study region conducive for formation of the system. It is to be noted that prior to the onset of the system, the lower atmosphere (up to $\sim$ 800 hPa) over the study area was characterised by the calm wind which was also seen in WPR observations (discussed in details in Sect. 3.2.4). This is an indication that boundary layer convection was instrumental in triggering the convective activity.

Wind from different directions (north-easterly flow in the NE sector of the study location and south-westerly flow associated with CC2 in the SW sector of the study location at $\sim$ 700 hPa) converged over the study area, making it favorable for the formation of the system. TIR1-BT recorded by INSAT-3D satellite shows the hourly evolution of cloud systems over the study area from 09:00 UTC to 14:00 UTC (Fig. 3). Red contour represents the region where the BT is less than 233 K, indicating the deep convective clouds. It may be noted that from 08:00 UTC onwards deep convective clouds started appearing along the convergence line (not shown in the figure), where the flows from different directions interacted with each other over the study area along with the significant influence of high terrain (discuss in details in Sect. 3.4.1). At 09:00 UTC a developing convective cloud band, elongated in the north-west to south-east direction, was observed in the satellite image at the north of the study area along with several scattered deep convective clouds nearby.

Eventually, these clouds developed and merged together and gave rise to a contiguous cloud system oriented in a north-west to south-east direction. During its lifecycle, the system moved south-westward due to the prevailing wind. The prevailing wind near the surface (below $\sim$ 850 hPa) was very feeble. Whereas the steady and persistent northerly/north-easterly winds at mid-level (i.e. $\sim$ 850 hPa and $\sim$ 700 hPa) had controlled the south-westward propagation of the system.

3.2. Observed Features and Thermodynamic Conditions

3.2.1 Meteorological Parameters Prior to the System

GPS-RS observation was taken at 08:04 UTC over Pune. Figure 4a represents the Skew-T plot from GPS-RS observation. Figure 5a, b shows the observed vertical profile (AGL) of temperature and relative humidity (RH) from GPS-RS and MWRP and Fig. 5c shows the vertical profile (AGL) of the mixing ratio (MR) from GPS-RS. The temperature and RH profiles from both from GPS-RS and MWRP are in good agreement.

These observations (from GPS-RS) indicated that prior to the formation of the system, the Convective Available Potential Energy (CAPE) value was significantly high (1739 J kg^{-1}), the CINE was extremely low and the lifting condensational level (LCL) was at 829 hPa pressure level. The detailed calculation of CAPE and CINE is provided in "Appendix". The high value of CAPE with a negligible amount of CINE made the atmosphere favourable for convection. A temperature inversion was observed at $\sim$ 725 hPa ($\sim$ 2.2 km AGL). The wind was predominantly weak westerly in the lower level (up to $\sim$ 825 hPa), weak northerly between $\sim$ 825 and $\sim$ 725 hPa and easterly above (above $\sim$ 725 hPa). The vertical extent of the westerly wind (Fig. 4a) matches with the region of high water vapor MR profile (Fig. 5c) indicating that the moisture got advected from the Arabian Sea along with the low-level westerly wind (which can also be seen in Fig. 2b). The sudden decrease in MR near $\sim$ 2.2 km indicates dry air intrusion by the northerly flow associated with AC. Above $\sim$ 2.2 km, water vapor
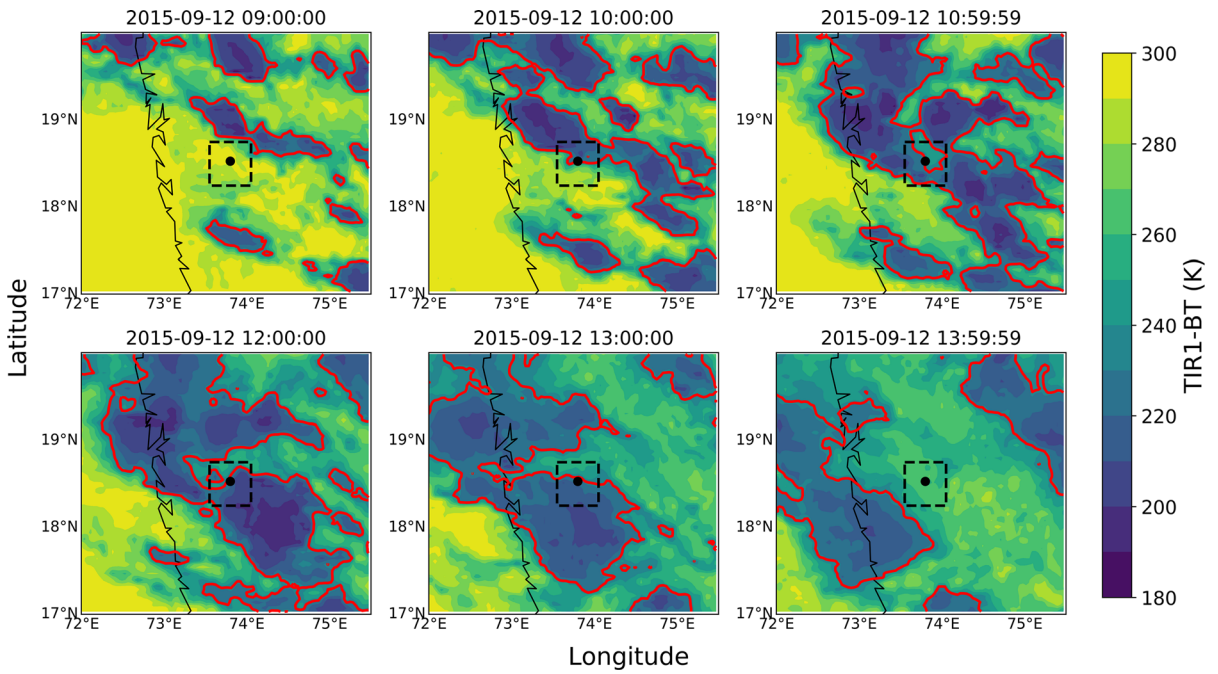
Figure 3
Evolution of convection as captured by INSAT-3D TIR1-BT. Red contours indicate the region of BT less than 233 K. The black dot and the dashed black box represent location of IITM premises and the 0.5° × 0.5° domain, respectively
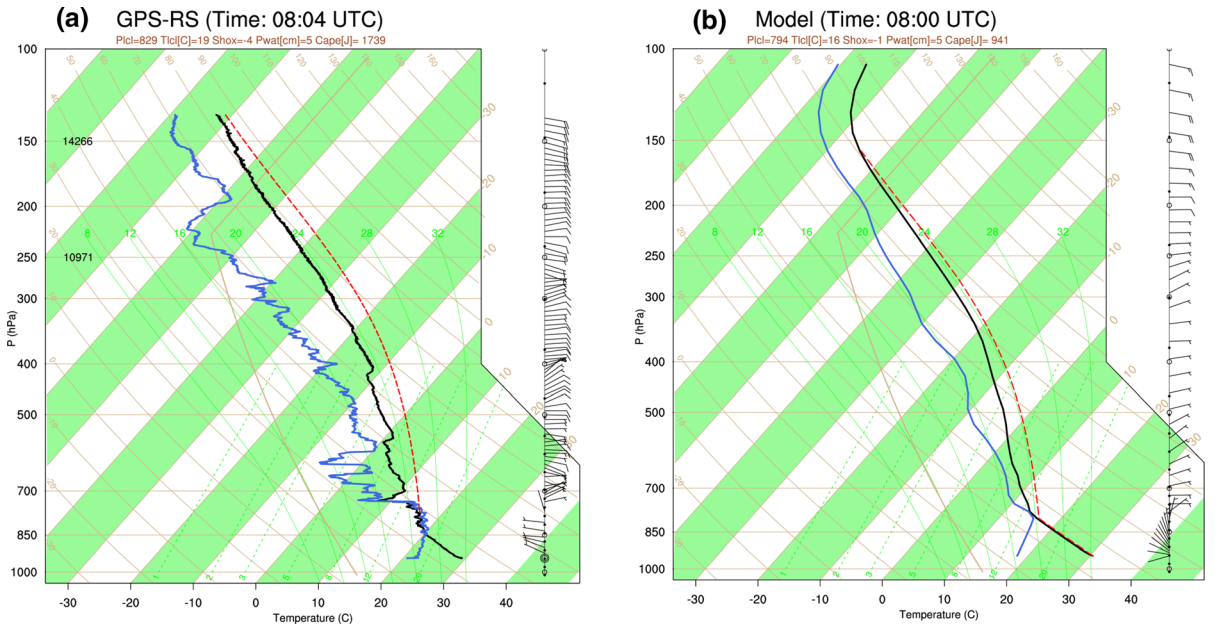

Figure 4
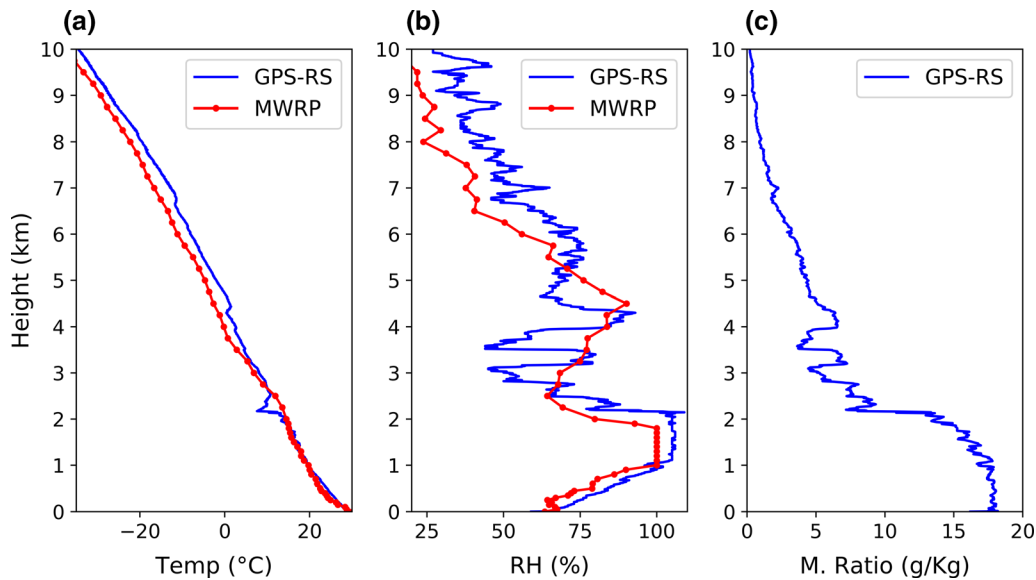Skew-T plot from **a** GPS-RS (at 08:04 UTC) and **b** WRF output (at 08:00 UTC) over Pune

Figure 5
Comparison of vertical profile (AGL) of **a** temperature and **b** relative humidity from GPS-RS (at 08:04 UTC) and MWRP (at 08:05 UTC) and **c** vertical profile (AGL) of mixing ratio from GPS-RS over Pune

MR showed oscillatory feature, which is indicative of gravity wave activity. RH gradually increased up to ∼ 1.2 km, being the boundary layer (BL) top and became saturated between ∼ 1.2 and ∼ 2.2 km, indicating that GPS-RS had gone through a cloud of 1 km thick, with cloud base of ∼ 1.2 km (or ∼ 1.7 km AMSL; further confirmed by LCL at 829 hPa) and the cloud extended up to ∼ 2.2 km (note that GPS-RS sensor has wetting issue and has registered more than 100% RH; meanwhile MWRP gives 100% RH). RH was quite low between ∼ 2.2 and ∼ 4 km. MR profile shows that below ∼ 2.2 km the MR was significantly high, almost 17 g kg^{-1} which suddenly reduced to ∼ 7 g kg^{-1} at ∼ 2.2 km and then decreased gradually with increasing height with a decrease in MR between ∼ 2.2 and ∼ 4 km. The RH and MR profile reveals that below ∼ 2.2 km the moisture content was remarkably high which showed a moist BL (MWRP derived PBL height was ∼ 1.5 km (AGL) just prior to the formation of the system; Fig. 7) and the moisture content was considerably low between ∼ 2.2 and 4 km which indicates a dry lower mid-troposphere, prior to the onset of the system. High moisture content in BL and relatively dry air above made the atmosphere

potentially unstable. The dry layer was also characterized by oscillations, as documented in RH (between 40 and 80%) and MR profile of GPS-RS observations, indicative of wave motions. The detailed characteristics of such wave motions over this location have been reported by Prabha et al. (2011). Good comparisons between the MWRP and GPS-RS for this case study as well as for the entire season (Balaji et al. 2017) illustrates that MWRP data can be used for detailed investigation of the system, including the thermodynamic parameters of interest.

3.2.2 Evolution of Surface Parameters and Cloud Base Height

Diurnal cycles of mean sea level pressure (MSLP), surface temperature, rainfall and cloud base height (CBH) during the evolution of the system are presented in Fig. 6a–c. Figure 6a shows the diurnal cycle of pressure from AWS on 11-Sept-2015, 12-Sept-2015, and 13-Sept-2015. Though the usual semi-diurnal patterns of MSLP are observed for each day, a stronger semidiurnal cycle is noticed on 12-Sept-2015. Prior to the onset of the cloud system, surface pressure was lower over the study region on 12-Sept-2015, compared to the preceding and
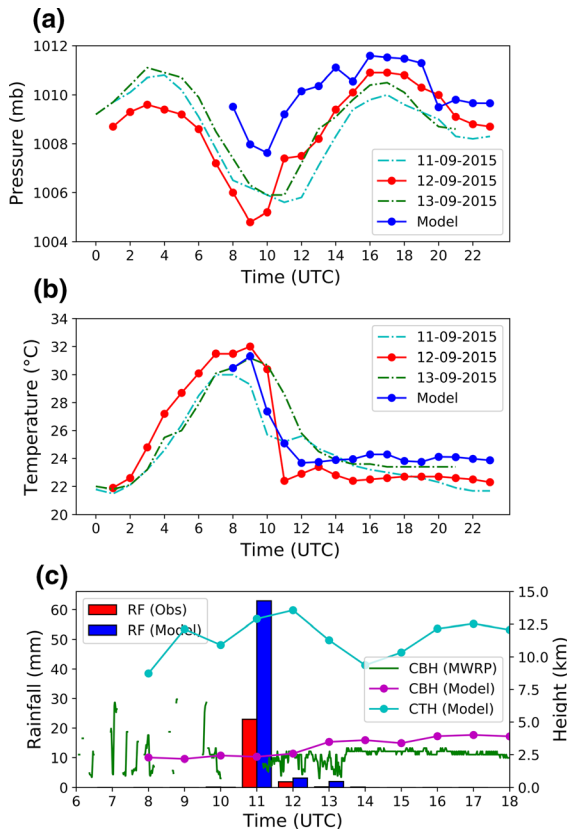
Figure 6

Comparison of observed and simulated **a** pressure, **b** temperature, **c** rainfall, CBH (AGL) and CTH (AGL). Simulated pressure, temperature and rainfall are taken from the model grid points which are nearest to the observation locations. Simulated CBH and CTH are spatially averaged over $0.5° \times 0.5°$ domain. CTH is not compared with observation

succeeding days. Low pressure was building up over the study region on 12-Sept-2015 and pressure continued to decrease from 05:00 UTC to 09:00 UTC until the incidence of the system at 10:00 UTC. This distinct behaviour was noted only on 12-Sept-2015, as on other days the lowest pressure was observed at 10:00–11:00 UTC at the time of maximum temperature. A small rise in pressure was observed at 11:00 UTC associated with the passage of meso high associated with the cloud system. After the incidence of the system, pressure had remained higher than other days, possibly due to the cold pool effect associated with the cloud cluster.

The temperature pattern shows (Fig. 6b) that daytime surface temperature on 12-Sept-2015 was higher than other days, during the hours until the

incidence of the cloud cluster at 10:00 UTC. A steep 9 °C drop in temperature, in a period of two hours, may be noted on 12-Sept-2015 over Pune. The minimum temperature (23 °C) was observed at 11:00 UTC which was maintained for several hours after the passage of the system. This sudden decrease in temperature might have been caused by the evaporation of precipitating particles in the sub-saturated environment and a cold pool was formed after the system passed over the area.

The observed surface rainfall as recorded by disdrometer is shown in Fig. 6c. It shows ∼ 23 mm rainfall occurred between 10:00 and 11:00 UTC in association with the cloud cluster and a very light rainfall was observed for successive 2 hours. The total amount (accumulated during the event) of precipitation recorded by the disdrometer was ∼ 25.50 mm. Disdrometer recorded instantaneous (temporal resolution: 30 s) rainfall intensity (Fig. 10b; described in details in Sect. 3.2.6) shows that the rainfall was convective (rainfall intensity > 15 mm/h) in nature between 10:08 and 10:57 UTC; which was followed by a very light stratiform rainfall up to 13:30 UTC. Figure 6c also represents the cloud base height (CBH) as registered by MWRP. MWRP provides CBH information at very high temporal resolution (roughly in 1 min interval). Prior to the onset of the system hardly any cloud was observed over the location. During the convective rain, the CBH information has been excluded due to the possible contamination in the data. The CBH was ∼ 2 km (AGL) during the stratiform counterpart of the system (up to 13:30 UTC) with significant undulation. The gradual increment in CBH was noted during the stratiform rain. After the rain event, CBH was observed at ∼ 2.5 km (AGL).

3.2.3 Evolution of Temperature and Vapor Density Profile

GPS-RS has provided only one-time vertical profile before the onset of the system, whereas MWRP has provided the continuous measurements (every ∼ 2 min) of the evolution of temperature and vapor density respectively along with the boundary layer height (PBL height) on 12-Sept-2015 (Fig. 7a, b). It shows that from 05:00 UTC onwards lower part of
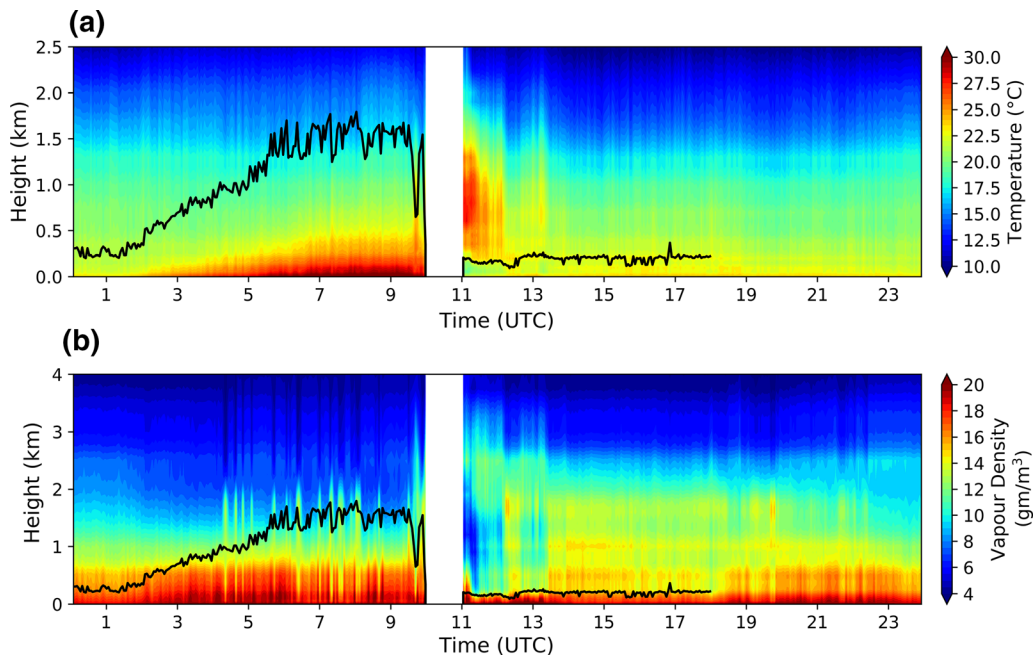
Figure 7
Evolution of MWRP recorded **a** temperature and **b** vapour density profile (AGL) on 12-Sept-2015. Black line indicates the PBL-height (AGL). The plots do not contain the data during convective rain

BL was warming, which continued up to 10:00 UTC (Fig. 7a), resulting in increased instability of the lower atmosphere and associated increase in PBL height. Usually, the lee side of WGs has less surface moisture content compared to the windward side. This has a strong bearing on the LCL height as air parcel over the lee side has to rise to a greater altitude for condensation. The day time BL over this region is described in Prabha et al. (2011), indicating the presence of convective thermals and rolls which are responsible for the BL exchange. High-resolution MWRP data reveal a similar feature during the present study. Well prior to the onset of the system (04:00 UTC onwards), an intermittent surge of moisture through thermals penetrating into higher altitudes were noted, which exchanged moisture into the relatively dryer middle levels. This moisture exchange in the lower part of BL can also be seen in the form of moist plumes rising above the BL (Fig. 7b), which indicates the moisture exchange from BL to free troposphere. These warm moist plumes became more intense just before the onset of the system, close to 10:00 UTC. Intermittent

updrafts–downdrafts and weak horizontal winds were the characteristics of the BL before the onset of the system over the study area (Fig. 8a, b; discussed in details in Sect. 3.2.4). Updrafts were associated with convective thermals and downdrafts made the BL dry. The PBL height increased gradually and from 06:00 UTC onwards it became 1.5 km (AGL) in height. MWRP data during the convective rain is removed from the analysis as MWRP data may not be accurate due to wetting of dome. Between 11:00 and 13:30 UTC a warm layer was observed between 0.5 and 1.5 km (AGL) (Fig. 7a) indicating the release of latent heat by the stratiform clouds. After the convective rain the lower atmosphere became cold which was associated with the cold pool, formed by evaporation of precipitating particles. This decrease in temperature was also noted in AWS data as discussed earlier. The PBL height reduced to a steady value of ∼ 250 m (AGL) after the convective rain. The time-height plots of vapor density profile show that the vapor density of the lower BL was significantly high more than 15 g m^{-3}, prior to the initiation of the convective precipitation. After the
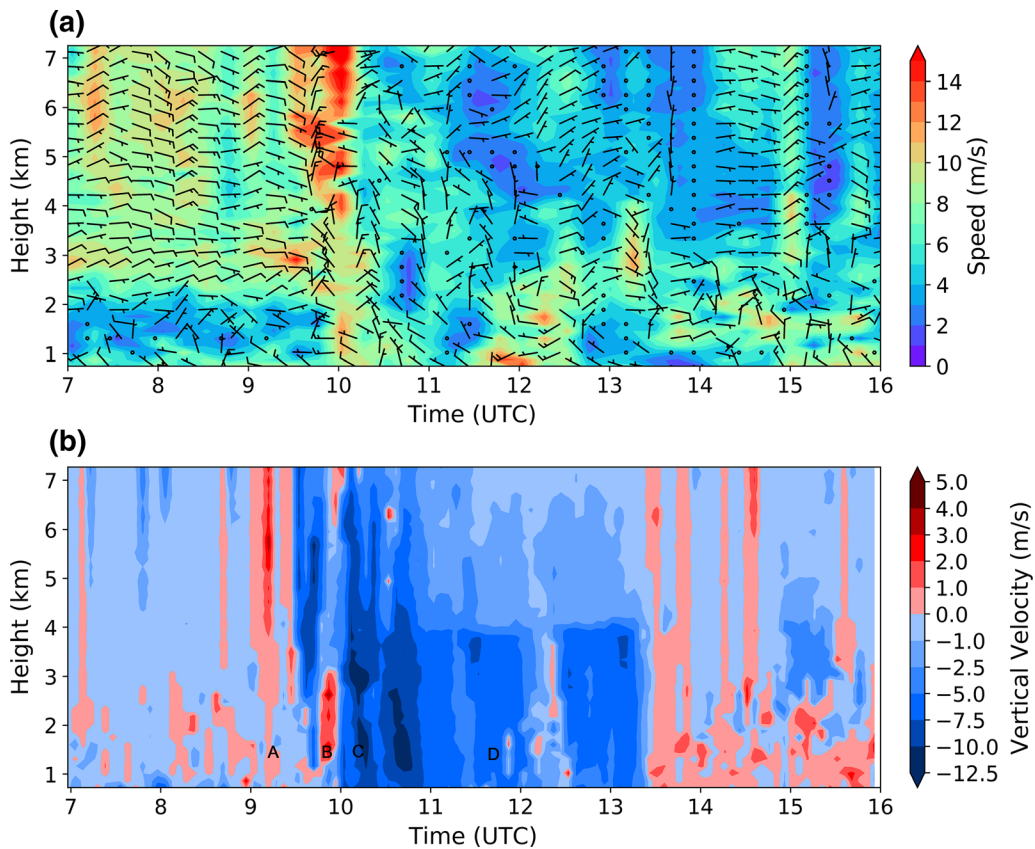
Figure 8
WPR observed **a** horizontal (15 min averaged) and **b** fall/vertical velocity. A, B, C and D represent the guest front, convective updraft, convective rain and stratiform rain, respectively. Heights are AGL

convective precipitation, the vapor density was considerably low within BL up to 13:30 UTC which might be attributed to the movement of the system.

The combined picture of temperature and vapor density as recorded by MWRP reveals that convective thermals and associated moist plumes transported moisture from BL to upper atmosphere prior to the initiation of the system. This increase in warm and moist air in the column happened during the daytime evolution as the BL was topped by shallow convective clouds of thickness of 1 km (also noted from GPS-RS data). This moisture exchange within BL and mid-atmosphere made it convectively unstable which is evident through the peak convection before the onset of the cloud cluster. The enhancement of this warm moist air in the column happened just before the initiation of the system, which may be instrumental in triggering deeper convection.

3.2.4 Horizontal and Vertical Wind

Analysing the synoptic conditions we have found that prior to the formation of the system, interaction of winds from different directions had occurred over the study area at all the levels up to 500 hPa, which included the advection of moist weak westerly at lower level, easterly wind at mid-level and dry northerly outflow of the anticyclone (over Rajasthan) at 850 hPa. Figure 8a, b represents the detailed structure of horizontal and vertical velocity and its evolution as recorded by the WPR. Details of inter-comparison of the wind measurements and associated errors are described in Balaji et al. (2017).

The horizontal component of wind reveals very calm condition over the study area up to $\sim$ 2 km (AGL) and feeble northerly component above it throughout the atmosphere till 01:00 UTC (not shown

in the figure), well prior to the system. From 01:00 UTC onwards, easterly flow with moderate intensity developed above $\sim$ 2 km (AGL) which persisted over the study region till the onset of the system (i.e. up to 10:00 UTC), whereas the lower level (below $\sim$ 2 km) remained calm. This calm BL (06:00 UTC onwards PBL height was $\sim$ 1.5 km AGL) possibly favored the transport of moisture in midlevel by intermittent convective thermals and associated moist plumes. After the passage of the system (14:00 UTC onwards), weak easterly was observed above $\sim$ 3 km (AGL).

Figure 8b shows vertical/fall velocity from the WPR. Prior to the onset of the system, intermittent updrafts and downdrafts could be seen in the lower troposphere (up to $\sim$ 2.5 km AGL). These updrafts were in association with the convective thermals and associated moist plumes transporting moisture to higher altitude (as seen in MWRP). A gust front was observed between 09:00 and 09:30 UTC, prior to the onset of the system as indicated by strong updrafts (indicated as 'A' in Fig. 8b). This was followed by downdrafts for nearly 20 mins duration. The updrafts were noted again when the system hit the location at 09:45 UTC with an increase in vertical velocity (indicated as 'B' in Fig. 8b). Vertical velocities at this point were close to 4 ms^{-1} within the lower $\sim$ 3 km (AGL). The precipitation started around 10:00 UTC and continued up to around 13:30 UTC. For first 1 h, the vertical extent of the fall velocity of hydrometeors was significantly high, reached more than 7 km (AGL) and the fall velocity was very intense, sometimes the falling speed of the hydrometeors crossed the speed of 12.5 ms^{-1}. This signifies that the initial rain was convective in nature (indicated as 'C' in Fig. 8b), which was followed by stratiform rain (indicated as 'D' in Fig. 8b). During stratiform precipitation, a prominent melting layer was observed at $\sim$ 4 km (AGL), and above this layer, a moderate fall velocity was observed which was possibly composed of snow and ice particles. These hydrometeors melted at about 4 km at the melting layer. The fall velocity of the precipitating particles was also less in the stratiform region, which hardly crossed 7 ms^{-1}. After the rain event, the system moved south-westward and WPR showed some updrafts that might be indicating the rain-free

dry air parcels advected over the study area. These could be associated with the residual BL.

3.2.5 Stability Indices

Several stability indices [i.e. CAPE, CINE, K Index (KI), KO Index (KOI), Thompson Index (TI), Total Totals (TT), Lifted Index (LI) and Showalter Index (SI)] have been analysed to understand the state of the atmosphere during the study period. These are calculated based on the temperature and humidity profile as recorded by MWRP. Detailed descriptions about these indices can be found in Cimini et al. (2015). The MWRP derived freezing level (FL) and wet bulb zero (WBT$_0$) level have also been examined. Data during the convective rain have been excluded because of the possible contamination.

CAPE was considerably high ($>$ 2500 J kg^{-1}) prior to the onset of the system (Fig. 9a) and continued to increase up to 09:00 UTC (not shown in the figure). A sudden decrease in CAPE was observed prior to the onset of the cloud cluster (09:30 UTC), indicating the formation of clouds. CINE was consistently low (almost zero) by this time, except a sudden decrease just prior to the onset of the cloud cluster. The unique feature was a sudden increase in the height of the FL and WBT$_0$ level just before the onset of the system as well as at the end of the convective rain (Fig. 9b). Increase in FL and WBT$_0$ level can be explained as follows: the cloud system was moving with a leading convective region and a trailing stratiform region by the prevailing wind. A gust front had developed at the leading edge due to the precipitation driven downdraft. Weak wind in lower troposphere, development of BL with peak convection in association with intermittent moisture transport above BL by convective thermals and development of the gust front, all together caused a sudden surge of moist air above BL, resulting in the increase in FL nearly to 4.5 km (AGL), just before the initiation of the system. Prior to the initiation of the convective rainfall, the WBT$_0$ level also rose and merged with FL indicating a deep saturated layer up to the FL. The increase in FL and WBT$_0$ level post the convective rain was possibly associated with the overturning circulations; a common feature associated with a mesoscale system and is the key process
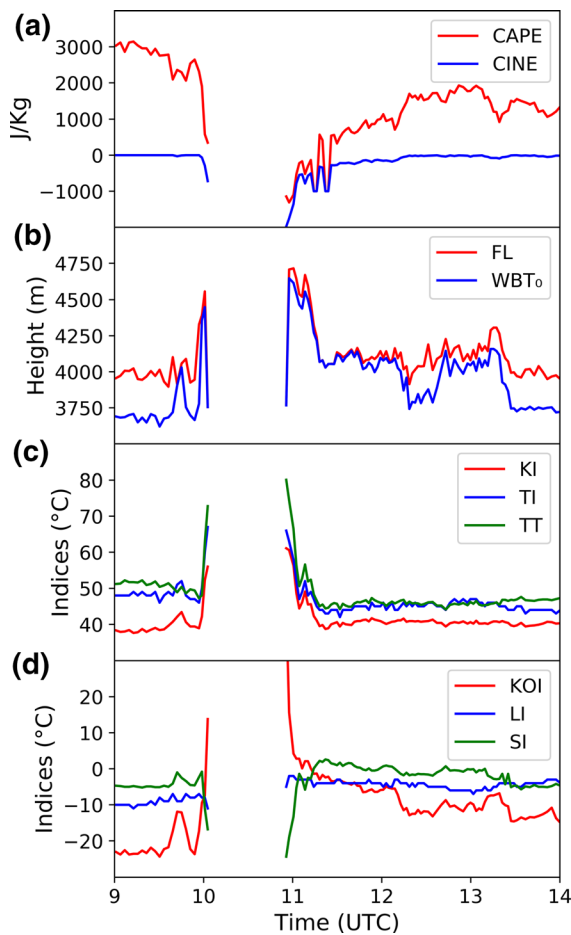
Figure 9
MWRP derived **a** CAPE and CINE, **b** freezing level (AGL) and WBT$_0$ level (AGL), **c** and **d** stability indices

for vertical mixing of air within the lower and mid/upper level. The ascending branch brings moist air from lower level to mid/upper level, whereas the descending branch brings dry air from mid/upper level to lower level. The slight separation in FL and WBT$_0$ level at the end of the convective precipitation is possibly associated with the warming caused by the overturning circulation in mid-level. Eventually, both FL and WBT$_0$ level came down to ~ 4 km and remained at that level up to 13:30 UTC. The co-existence of FL and WBT$_0$ level in close vicinity (up to 13:30 UTC) indicates that the layer was almost saturated.

High KI value (~ 40) prior to the onset of the cloud cluster (Fig. 9c) reflected the instability between the top of the BL and 500 hPa and/or high

moisture content at 850 and/or 700 hPa. High TI value (> 45) before the onset of the system (Fig. 9c) represented increased instability between 850 and 500 hPa and/or increased moisture content below 700 hPa, which in turn indicates the favourable condition for cloud formation. TT represents the combination of Vertical Totals, i.e. static stability between 850 and 500 hPa and Cross Totals, i.e. the moisture content at 850 hPa. Prior to the onset of the system the TT value was quite high (~ 50) which indicated high moisture content at 850 hPa and/or decrease in static stability between 850 and 500 hPa (Fig. 9c). Negative value of KOI, LI and SI indicates higher moisture content in lower level (i.e. below 850 hPa and/or within BL). Prior to the onset of the system the negative value of KOI (< − 20), LI (close to − 10) and SI indicated ample amount of moisture content in the lower troposphere which was quite favorable for convection to occur (Fig. 9d). In post convective rainfall (after 11:00 UTC) the gradual decrease of KOI till 13:30 UTC (end of stratiform rain) indicated an increased moisture content in lower level, possibly due to the formation of the cold pool (also confirmed by AWS and MWRP). During this time the SI became positive and remained close to zero up to 13:30 UTC which shows the stability of 850 hPa level after the heavy rain.

3.2.6 Evolution of the Cloud System and Lightning

Figure 10a shows the evolution of the cloud cluster (reflectivity) as observed by radar (CAPPI at 5 km AMSL) at different time (from 08:56 to 13:06 UTC). It can be seen that by 08:56 UTC a multicore convective cloud cluster was present to the north of the study location (indicated by black star) which eventually propagated south-westward. By 09:34 UTC a new convective cell started forming exactly over the study location, grew up significantly by 09:59 UTC and merged with the multicore convective cluster by 10:36 UTC, which gave rise to a contiguous convective cloud cluster of more than ~ 100 km in length with leading convective and trailing stratiform clouds (as seen by reflectivity value). Another convective cluster started forming in the south-east sector of the former cloud system, grew and eventually merged together and gave rise to
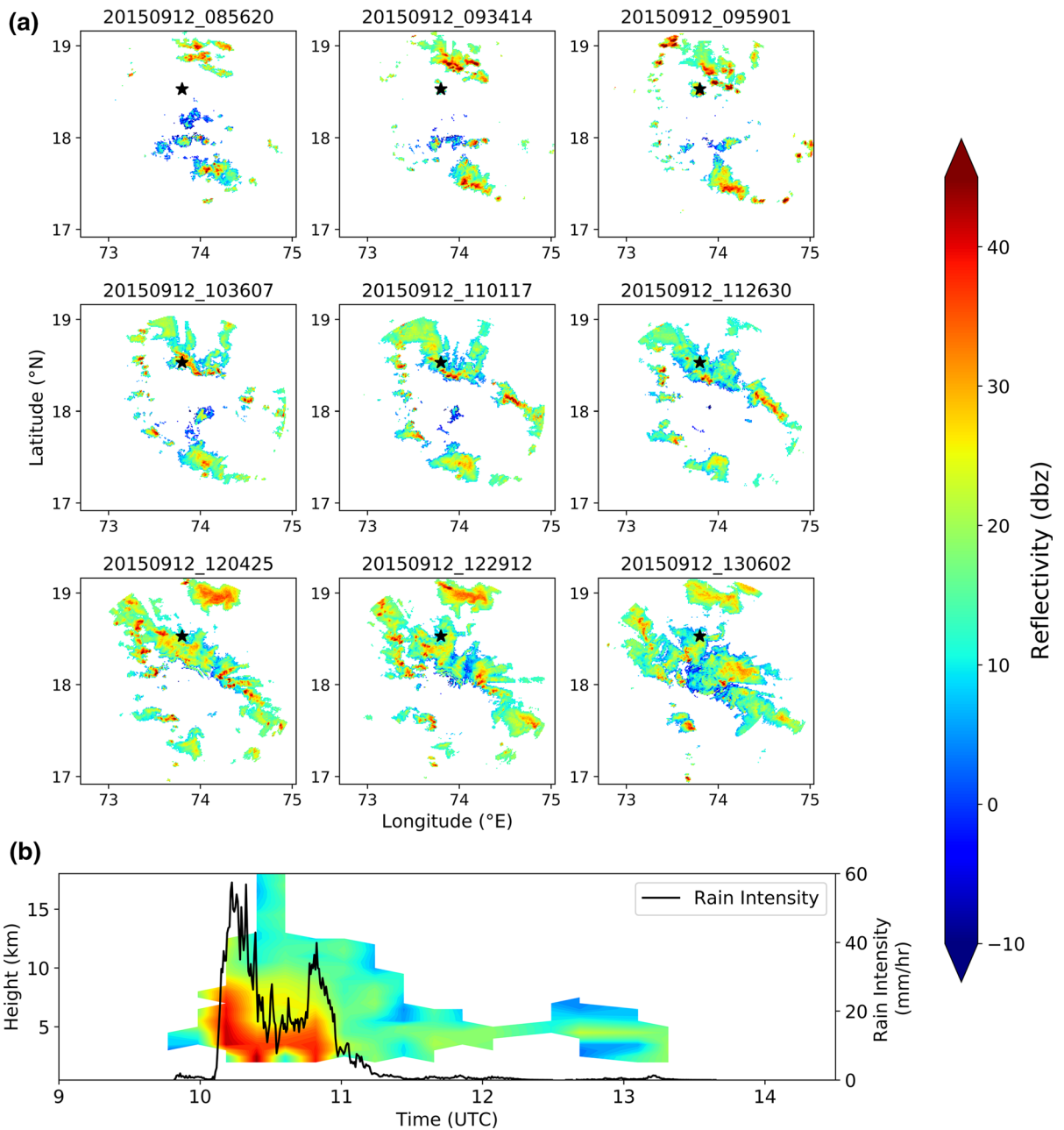
Figure 10
a Evolution (half-hourly) of the cloud system as observed by Radar (CAPPI at 5 km AMSL) between ~ 09:00 and ~ 13:00 UTC.
b Evolution of radar observed vertical profile (AGL) of reflectivity over IITM and co-located disdrometer recorded instantaneous (temporal resolution: 30 s) rainfall intensity (as secondary Y-axis)

a linear convective cluster oriented in north-west to south-east direction over the study location by 11:26 UTC, with leading convective and trailing stratiform clouds. Eventually these cloud system developed and gave rise to a contiguous area of stratiform clouds with embedded multiple convective cores within it. It is worth noting that the INSAT-3D satellite has observed the evolution of the top of this cloud cluster

and is shown in Fig. 3. This is a rare and unique event of a rain bearing cloud cluster over the rain shadow region of the WGs which has been well-probed by several state of the art instruments. The cloud cluster had propagated from north-east to south-west direction over the study region during its lifecycle.

Figure 10b shows the vertical variation of reflectivity over Pune (indicated as black star in Fig. 10a and blue triangle in Fig. 1b). The secondary Y-axis represents the instantaneous rainfall intensity (temporal resolution: 30 s) recorded by disdrometer (located at the black star). Deep convective clouds (reflectivity > 35 dBZ) might be noted over the study location between 10:00 and 11:00 UTC with two intense cores and the vertical extent of the clouds crossed $\sim$ 12 km (AGL). This was followed by stratiform clouds. The disdrometer recorded rainfall intensity shows that the convective rainfall (rainfall intensity > 15 mm/h) started at 10:08 UTC and ceased at 10:57 UTC, and the maximum value of rainfall intensity recorded by disdrometer was $\sim$ 60 mm/h. The convective rainfall over the study location was associated with the two convective cores; which was followed by a very light stratiform rainfall up to 13:30 UTC.

Figure 11a shows the spatial distribution of Cloud to Cloud (CC) and Cloud to Ground (CG) lightning activity and Fig. 11b shows the CC and CG lightning counts per minute in the 1° × 1° domain (as indicated by a solid red box in Fig. 1b) over the study area between 08:00 and 15:00 UTC. The lightning activity propagated from north-east to south-west direction over the study area as time progressed (Fig. 11a), which indicates the direction of propagation of the deep convective clouds. It also gives an indication that these cloud bands were formed north and north-east of Pune at 09:00 UTC and were propagating over the region. Maximum lightning (both CC and CG) over the domain was observed between 09:00 and 10:00 UTC and eventually both the number decreased. Total 1684 CC and 358 CG lightning strikes were recorded by the LLN sensors between 08:00 and 15:00 UTC over the domain. The lightning activity indicates the associated charged processes within the cloud systems.
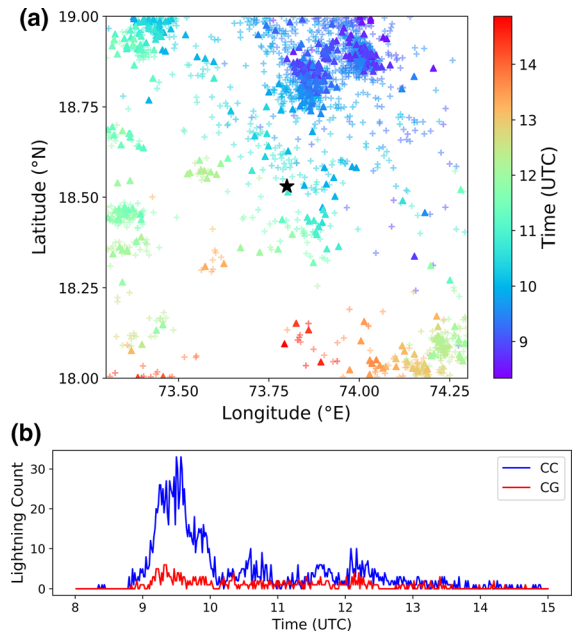

Figure 11
Lightning activity over 1° × 1° domain between 08:00 and 15:00 UTC (black star denotes location of IITM premises). **a** Spatial distribution of lightning (Plus and solid triangle represent CC and CG lightning respectively, colorbar represent the time of lightning) and **b** lightning counts per minute

3.3. Comparison of Observation with Simulation

Figure 4a, b shows observed and simulated Skew-T plot from GPS-RS and WRF model at 08:04 UTC and 08:00 UTC respectively over Pune. Both show weak westerly wind up to $\sim$ 825 hPa, weak northerly wind between $\sim$ 825 and $\sim$ 725 hPa and easterly above $\sim$ 725 hPa. The GPS-RS and WRF simulated LCL is observed at 829 hPa and 794 hPa pressure level, respectively. In both the cases, precipitable water is 5 cm. The GPS-RS observed CAPE is 1739 J kg^{-1} and the WRF simulated CAPE is 941 J kg^{-1}. It is evident from the Skew-T plot that the model has underestimated most of the parameters in the simulation.

In Fig. 6a, b we have compared the WRF simulated pressure (MSLP) and temperature (at 2 m) with the AWS recorded pressure (MSLP) and temperature on 12-Sept-2015. We have chosen the simulated pressure and temperature at the model grid point which is nearest to the AWS location (shown as a red star in Fig. 1b) and compared with observed parameters. The simulated MSLP shows a similar

pattern as the observed MSLP with overestimated intensity on 12-Sept-2015 (Fig. 6a). The simulated temperature on 12-Sept-2015 is also in good agreement with the observed temperature (Fig. 6b). The sharp decrease in temperature during the rain event and the formation of a cold pool have been properly captured by the model.

Observed and forecasted hourly rainfall is presented in Fig. 6c. The simulated rainfall has been chosen at the model grid point closest to the ID location (shown as a blue triangle in Fig. 1b). It is worthwhile to note that the initiation of the convective rainfall has been forecasted well by the model with overestimated value. It is to be noted that the ID measures the rainfall at a particular location (point observation), whereas the simulated rainfall is the 1 km × 1 km averaged rainfall at the model grid point closest to the ID. Figure 6c also contains the comparison of observed and simulated ($0.5° \times 0.5°$ spatial averaged) CBH (i.e. lowest altitude where $Qc > 0.01$ g kg^{-1}) and the variation of cloud top height (CTH, i.e. highest altitude where $Qc + Qi + Qs + Qg > 0.005$ g kg^{-1}) over the study area. CBH is higher in the model compared to MWRP observations. Both CBH and CTH shows that from 08:00 UTC onwards the cloud started forming over the domain and maximum cloud thickness was observed between 10:00 and 12:00 UTC which subsequently reduced.

To examine the detailed structure of the initiation, organization, and evolution of the system we have compared the time lapse images of reflectivity from radar and WRF output. Figure 12b, d represent the simulated reflectivity (horizontally sliced near 5 km AMSL) at 10:00 UTC and 12:00 UTC respectively and Fig. 10a, c show the corresponding observed radar reflectivity (CAPPI at 5 km AMSL) at 09:58 UTC and 12:03 UTC, respectively. The cloud organization was reasonably captured by the model at 10:00 UTC with slightly over estimated intensity and modified shape (from Fig. 12a, b). The simulated clouds seem to be organized along the Western Ghats. At 12:00 UTC the spatial cross section of reflectivity shows the large coverage of the cloud with slight over estimated intensity (from Fig. 12c, d). The model and observational differences in the reflectivity could be attributed to the spatio-temporal

differences of cloud system simulated by the model. However, the overestimation of simulated reflectivity is possibly due to the microphysics scheme which has been reported by earlier studies (Segele et al. 2013; Hagos et al. 2014; Min et al. 2015; Song and Sohn 2018) and possibly due to the high graupel amount in upper level (Song and Sohn 2018). Figure 12e, f show the spatial distribution of observed (IMERG) and WRF forecasted (regridded into IMERG grid) accumulated (between 09:00 and 17:00 UTC) precipitation, respectively. It can be seen that the model forecast has overestimated the precipitation with slight spatial mismatch.

3.4. Simulated Characteristics of the Cloud System

3.4.1 U, θ_E and Favourable Location of Initiation

$1° \times 1°$ domain averaged (as indicated by a solid red box in Fig. 1b) zonal wind (U) is shown in Fig. 13a, which indicates that the wind was predominantly westerly in the lower level and easterly above (also verified from ERA-Interim reanalysis data GPS-RS and WPR). The strength of the easterly wind increased with altitude. The low-level westerly winds brought moisture from the Arabian Sea which could have strengthened the system. The $1° \times 1°$ domain averaged equivalent potential temperature (θ_E) is presented in Fig. 13b. It shows that there was a significant gradient in θ_E at the lower atmosphere (up to ~ 5 km) prior to the onset of the system (up to 10:00 UTC), which made the lower atmosphere convectively unstable. The high θ_E value prior to the onset of the system indicates the warming of BL and moisture intrusion in the lower level by the westerly wind. As the system crossed the study location, θ_E decreased in the lower level, which might be a cause of cold pool formation where the temperature got reduced due to the evaporation of precipitating particles.

To identify the favorable location for the initiation of the system, we overlaid the contour of 35 dBZ at nearly 2 km (AGL) with the terrain height (Fig. 14). The 35 dBZ threshold indicates the deep convective clouds. It shows, during the early stage of formation of the system (08:00 and 09:00 UTC); the convective cells were scattered randomly, but preferentially
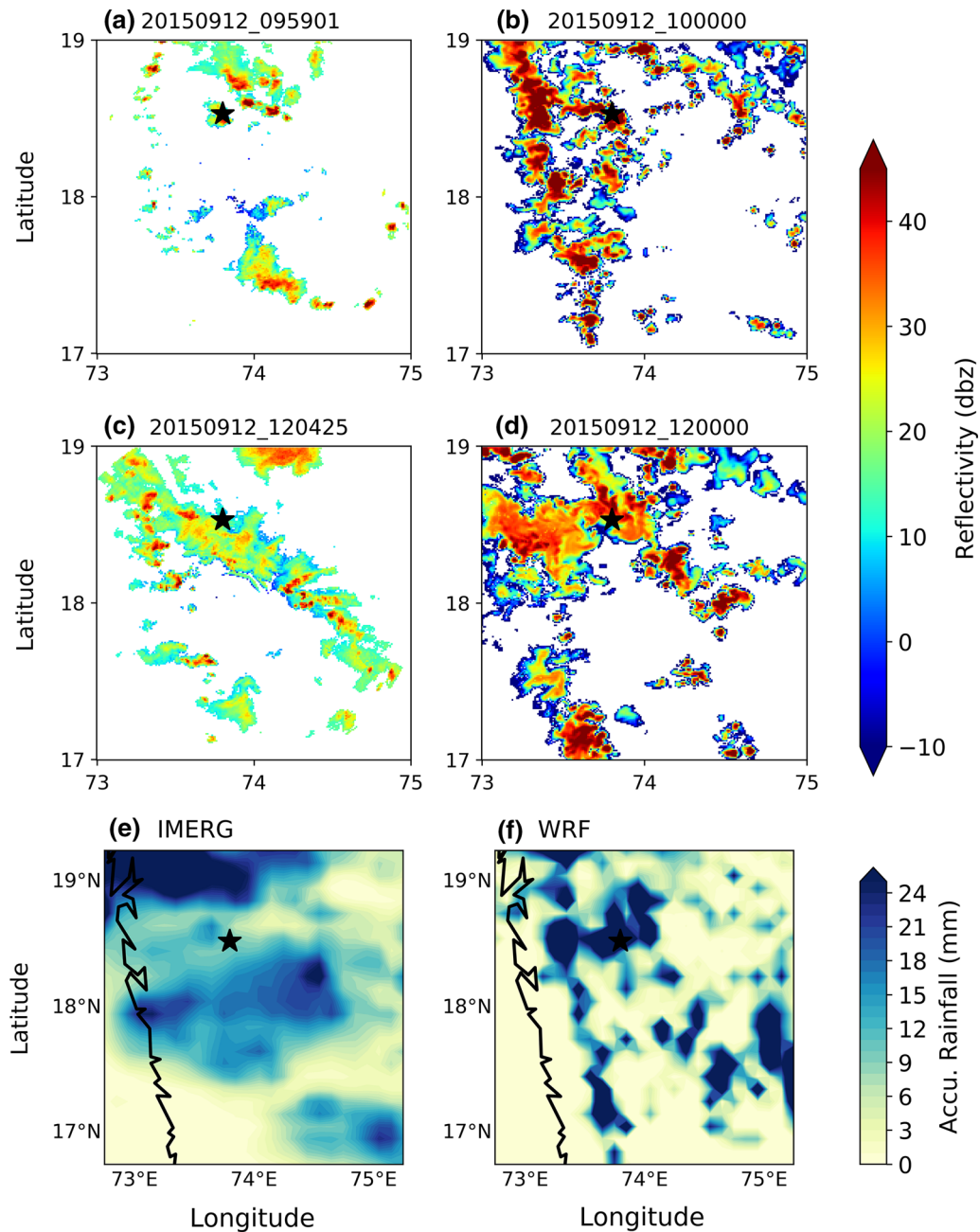
Figure 12
Comparison of observed and simulated **a–d** reflectivity at ∼ 5 km (AMSL) and **e–f** spatial distribution of accumulated rainfall (between 09:00 and 17:00 UTC). **a** CAPPI at 09:58 UTC, **b** reflectivity (WRF) at 10:00 UTC, **c** CAPPI at 12:03 UTC and **d** reflectivity (WRF) at 12:00 UTC. Accumulated rainfall from **e** IMERG and **f** WRF (regridded into IMERG grid). Black star represents the location of IITM

occurred over the hilly area with an average terrain height between 600 and 900 m. These isolated cells eventually developed and merged together and

produced a contiguous area of thick clouds. The observed system over Pune was part of such convective band with several convective cells embedded
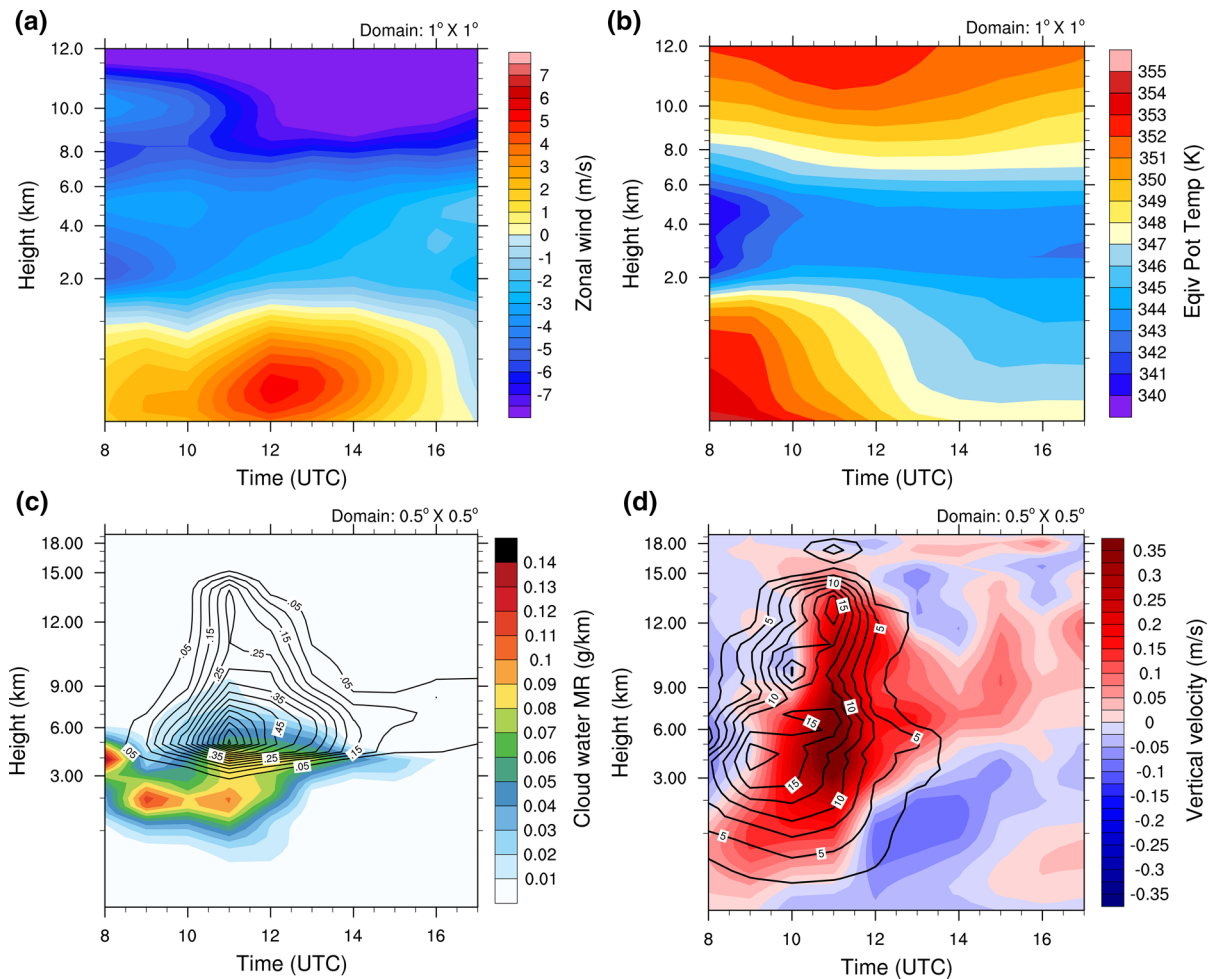
Figure 13
Simulated **a** zonal wind, **b** equivalent potential temperature, **c** mixing ratio (color shade represents cloud water mixing ratio and contours represent cumulative mixing ratio of solid hydrometeors i.e. ice, snow and graupel) and **d** vertical velocity (colorbar represents the average vertical velocity and black contour lines represents the maximum vertical within the domain). Heights are AGL

within it, which is also confirmed by INSAT-3D BT (Fig. 3) and radar (Fig. 10a) observations.

3.4.2 Mixing Ratio, Vertical Velocity and CFAD of the Cloud System

Figure 13c, d shows the distinct evolution of WRF simulated mixing ratio (color shade represents cloud water mixing ratio and contours represent cumulative mixing ratio of solid hydrometeors i.e. ice, snow and graupel) and vertical velocity (color bar represents the average vertical velocity and black contour lines represent the maximum vertical within the domain)

respectively, over $0.5° \times 0.5°$ domain (shown as dashed red box in Fig. 1b) over the study area. Figure 13c, d indicate that from 09:00 UTC onwards shallow clouds (predominantly warm clouds, with slight mixed phase contribution) started forming over the domain. Significant amount of mixed phase cloud was observed by 10:00 UTC with moderate domain averaged updraft up to ~ 9 km (AGL). Intense mixed phase was observed at 11:00 UTC in association with maximum domain average updraft and the cloud system attained its maximum height by this time, extended vertically up to ~ 15 km (AGL), along with the peak intensity of the observed surface
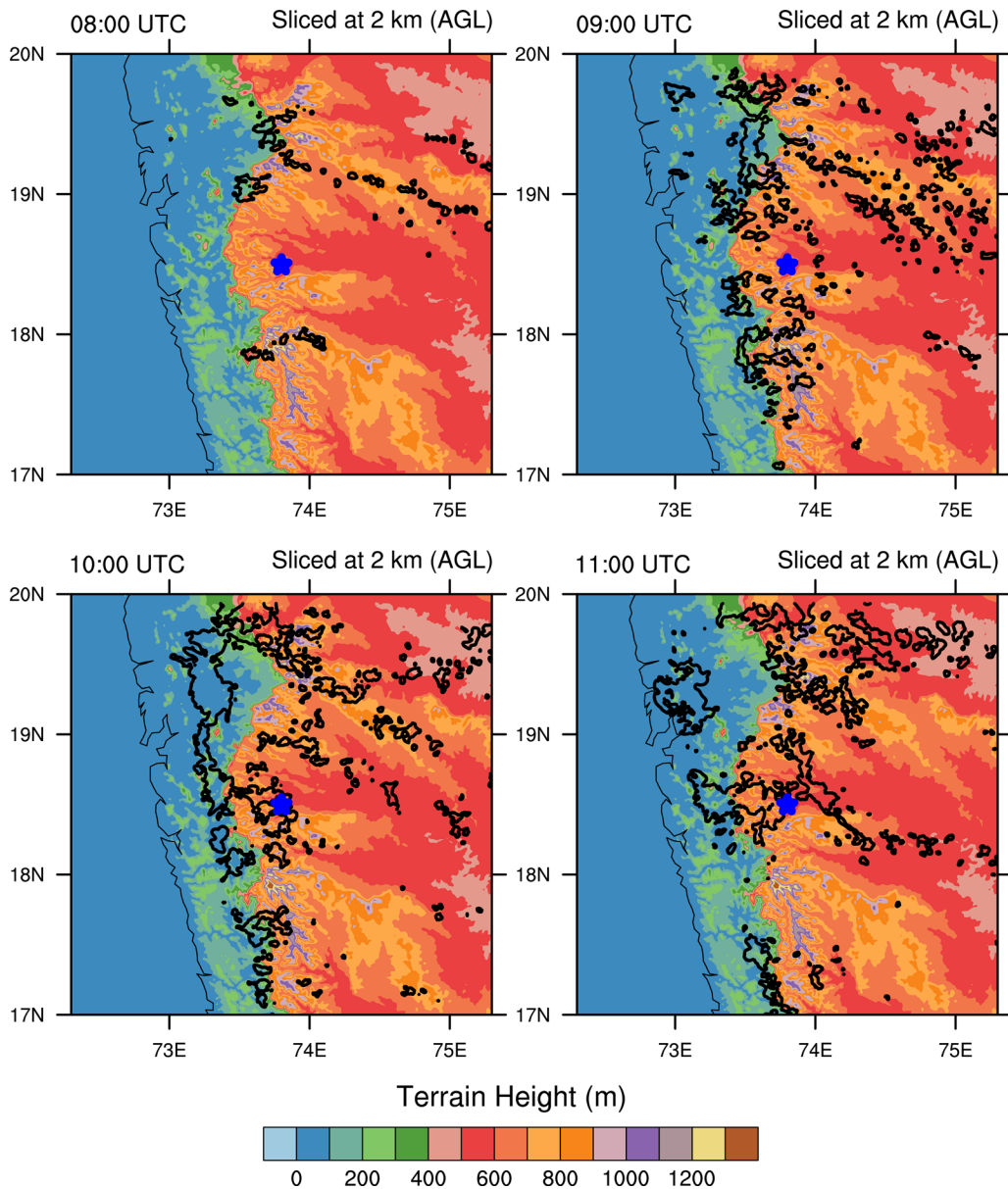
Figure 14
Terrain height overlay with reflectivity contour (of 35 dBZ) sliced at 2 km (AGL). Blue star indicates the location of IITM

rainfall (Fig. 6c). The maximum vertical velocity over the domain (black contours in Fig. 13d) shows the presence of intense updraft core(s) (vertical velocity greater than 12.5 ms^{-1}) between ~ 2 and ~ 7 km from 09:00 UTC onwards, which gradually increased in height and reached up to ~ 14 km by 11:00 UTC, indicating the convective part of the system. From 12:00 UTC onwards, mainly the solid hydrometeors (i.e. ice, snow and graupel) persisted over the domain in association with moderate domain averaged updraft, indicating the stratiform counterpart of the system.

Contoured frequency by altitude diagram (CFAD) represents the frequency of occurrence (in percentage) of a particular value of reflectivity for a particular height. Figure 15 shows the CFAD of

simulated reflectivity (with bin interval of 2 dBZ) for different time steps over 0.5° × 0.5° domain (shown as a dashed red box in Fig. 1b). At 09:00 UTC, the frequency of occurrence of reflectivity covers a wide range of values, showing maxima between 20 and 40 dBZ, indicating the formation of clouds and slight drizzle. At 10:00 UTC the maximum occurrence of reflectivity centered towards 40 dBZ and extending up to ground represented the deep convective clouds with a heavy convective downpour. The vertical growth of the cloud with heavy rainfall was observed at 11:00 UTC. With increasing height, the probability of high reflectivity gradually decreased, possibly due to entrainment induced evaporation of hydrometeors, as well as due to rain. A higher percentage of shallow clouds in the area also lead to this behaviour. The cloud top entrainment instabilities lead to depletion of the cloud. At lower levels, the shallow clouds assisted by collision coalescence and precipitating cells increased reflectivity. A secondary maxima of the frequency of reflectivity, ranging between − 20 and 20 dBZ, was observed at 12:00 UTC at the altitude ranging from 11 to 14 km, indicating the formation of the anvil, along with the primary weakening patch centered at 40 dBZ. From 13:00 UTC onwards the system started reducing its strength significantly. The signature of formation of the

melting layer is evident from 12:00 UTC onwards as the sudden enhancement of frequency of occurrence of reflectivity at 4 km; the presence of melting layer was clearly observed at 13:00 and 14:00 UTC as there was a sudden shift in maxima of occurrence frequency of reflectivity at 4 km. Above the melting layer, the maxima are due to the presence of small snow particles, and below, due to the rain drop which is generally larger in size compared to the ice particles. This sudden change in hydrometeor size caused a sudden shift in reflectivity maxima. The cloud system hardly caused any rain from 14:00 UTC onwards and persisted as weak stratiform clouds over the domain.

3.4.3 Microphysical Evolution of the Cloud System

Another objective of this study is the analysis of the evolution of the microphysical properties of the cloud system. We have used WDM6 microphysics scheme, which uses water vapor along with five hydrometeors populations, i.e. cloud droplets, ice, snow, rain, and graupel. It simulates the mixing ratio for water vapour and all the five hydrometeor species and provides additional information about the number concentration of cloud droplets and rain drop. This scheme accurately distinguishes the rainfall and microphysical differences between the convective
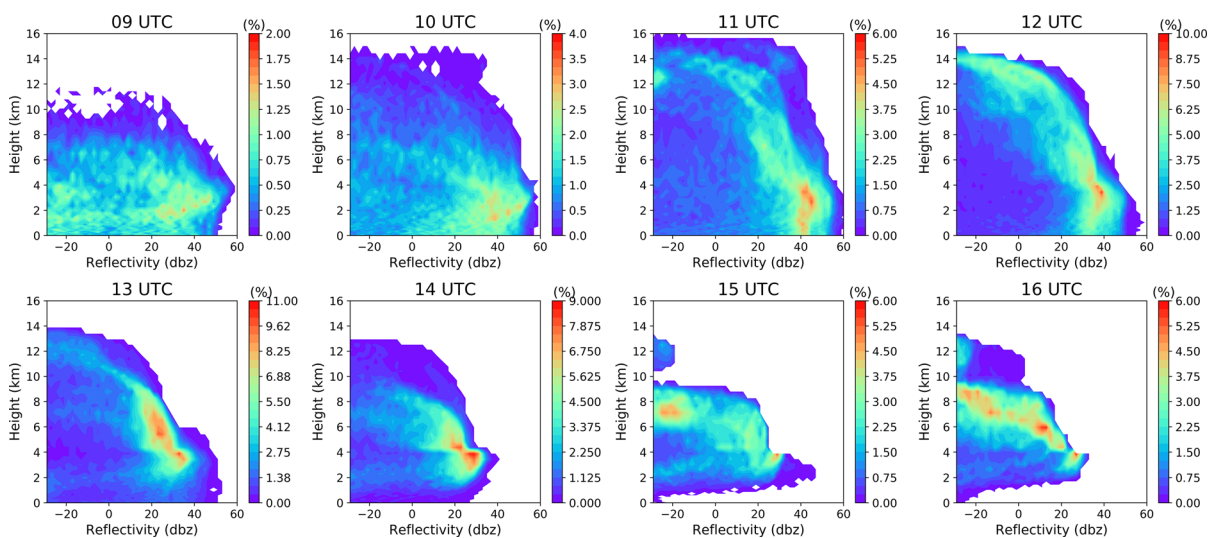

Figure 15
CFAD of WRF simulated reflectivity over 0.5° × 0.5° domain for different time. Heights are AGL

and stratiform region of a mesoscale system. It is able to capture the radar bright band which indicates the melting layer near the freezing level.

The presence of five hydrometeor classes can be attributed to different microphysical processes associated with the system (this inference is inspired from Wu et al. (2018)). Ice crystals generally form due to vapor deposition. Aggregation is the primary process where several ice crystals stick together and form snow. Condensation of water vapor is the primary process for formation of cloud droplets, but in rare occasions melting of ice crystals may also generate cloud droplets. Graupel is generally formed due to riming process in the presence of supercooled liquid water. In presence of strong updraft, cloud droplets are transported well above the freezing level and when these super cooled droplets come into contact with snow/ice particles, it freezes through riming. Occasionally droplet freezing can also produce graupel. Rain drops primarily form through two processes; collision–coalescence of cloud droplets and melting of graupel (and occasionally snow). So the variation of mixing ratio of the five hydrometeors can provide a detailed insight of the on-going microphysical processes at different time step during the lifecycle of the system.

Figure 16 shows the evolution of mixing ratio of different hydrometeor species within $0.5° \times 0.5°$ domain (shown as a dashed red box in Fig. 1b) over the study area. Initially, the clouds formed as shallow cloud and by 09:00 UTC the rain mass started reaching the surface as attributing to the warm microphysical processes (collision–coalescence). A very small amount of ice crystals were formed due to vapor deposition in the homogeneous ice region close to 12 km. There was a spontaneous transformation to mixed phase cloud with a significant increase in graupel mass which melted and contributed to rain water. At 10:00 UTC the graupel mixing ratio increased significantly in association with the high domain averaged updraft (Fig. 13d) and the super cooled liquid water (i.e. cloud water mixing ratio) up to 9 km, which indicates the enhancement in riming process. There was a prominent indication of the increase in primary ice and snow which indicates the on-going vapor deposition and aggregation process. Rain water mixing ratio, which is primarily generated

due to the melting of graupel, increased significantly in the lower level. Maximum graupel mixing ratio (at 5.8 km) was observed at 11:00 UTC along with super cooled liquid water up to 10 km and maximum domain averaged updraft (Fig. 13d), indicating further enhancement in riming process. The double peaks in graupel are attributing to strong updrafts transporting graupel at higher altitudes. Super cooled liquid might have got transported to the upper level through these strong updrafts. The cloud system achieved the highest vertical extent by this time and was also associated with the peak in surface rainfall (both observed and simulated). Significant enhancement in ice crystals and snow was observed at the upper level, indicating the further enhancement in vapor deposition and aggregation process. Maximum rain (at 3 km, where graupel and other ice mass go to zero and complete melting happens) and cloud water mixing ratio were also observed at this time indicating the maximum melting and collision–coalescence process. At 12:00 UTC maximum ice and snow mixing ratio was observed in the upper level, which is associated with the formation of the anvil as noted in the CFAD of reflectivity (Fig. 15). This shows that the highest vapor deposition and aggregation process can be noted during the formation of the anvil. The graupel and rain mixing ratio started decreasing by this time, as the stratiform region developed. Rainwater mass decreased concurrently with graupel mass. The trailing period of the cloud cluster was dominated by snow and pristine ice (indicating the vapor deposition and aggregation processes in the residual clouds), which gave rise to negligible rain mass on melting.

During the lifecycle of the system, graupel is found to be the dominant ice hydrometeor type. Generation of graupel through riming seems to be the dominant microphysical process and melting of graupel is the primary source of rainwater. Super cooled liquid water was present throughout the system and peaked when graupel mass was maximum. The concurrence of super cooled liquid and graupel in association with maximum updraft was favorable for production of charges in the system, which is also seen as observed lightning activity.
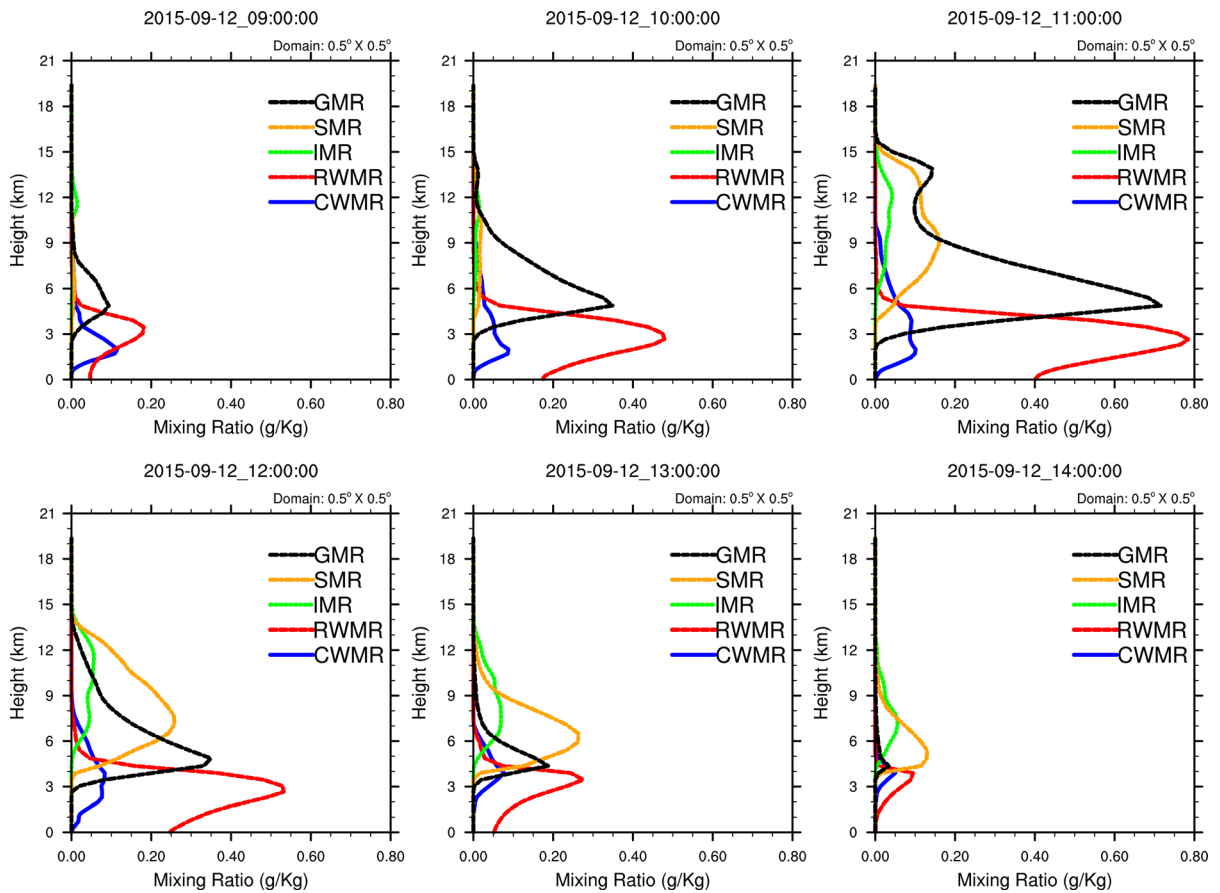
Figure 16
Evolution of Hydrometeors over 0.5° × 0.5° domain (GMR, SMR, IMR, RWMR and CWMR represent graupel mixing ratio, snow mixing ratio, ice mixing ratio, rain water mixing ratio and cloud water mixing ratio, respectively). Heights are AGL

4. Summary and Conclusions

The main focus of this study is to critically analyse the convective activity on 12-Sept-2015 over Pune, covering the dynamical, thermodynamical and microphysical aspects, by making use of a variety of observations and numerical simulation. Detailed analysis of such cloud cluster, using different types of high-resolution observational platform and numerical simulations, is hardly available over this location. Initiation and evolution of the cloud system with favorable background conditions have been fore-casted with considerable accuracy by WRF model at a cloud-resolving scale of 1 km and the event has been simultaneously probed with various state of the

art instruments; both together provides detailed insight about the characteristics of the cloud system.

Large scale features played the key role in the formation of the cloud system over the rain shadow region in the leeward side of WGs which is also consistent with the findings of Murthy et al. (2018). Weak lower level moist westerly and further inci-dence of moisture incursion from Arabian Sea were crucial for the triggering of convection. The mid-level dry air incursion from the north further made the location conducive for formation of the deep cloud system. The intermittent convective thermals were observed in the BL prior to the onset of the system and associated moist plumes transported moisture above the BL. Initial hours during the day was characterized by shallow clouds that were

triggered due to BL convection. Subsequently south-westerly winds had increased and the moisture front had arrived at the site, which allowed parcel ascent to greater depths across the dry layer that was present. The large scale conditions favoured introduction of more moisture in the upper layers, which favoured triggering of deeper convection. Pronounced wind shear in the low-level helped the cloud system to orient in north-west to south-east direction and the cloud cluster moved towards the south-west direction due to the prevailing wind.

Onset of the system occurred over the study area at about 10:00 UTC and continued up to 11:00 UTC as convective rain, followed by a stratiform counterpart which continued up to 13:30 UTC. Well prior to the onset of system the lower troposphere (up to ~ 2 km) was convectively unstable and several stability indices were beyond the precursor conditions for severe thunderstorm convective activity (CAPE was greater than 2000 J kg^{-1} and CINE was close to zero). The unique feature observed close to initiation of the system was the sudden increase in FL and WBT$_0$ level, caused by a sudden surge of warm and moist air into the mid-level. To the best of our knowledge, this has not been reported earlier and there is hardly any literature available on this feature. The transitioning features of lowering FL and elevated WBT$_0$ level were also recorded.

The cloud system started with warm rain processes and eventually developed into a mixed phase cloud system. During the convective rain, maximum precipitation came from the mixed phase through melting of graupel. At the same time, the supercooled liquid was seen up to ~ 10 km in association with strong updrafts which facilitated the formation and growth of graupel by riming. The co-existence of supercooled liquid and other ice hydrometeors (i.e. ice crystal, snow, and graupel) indicates charged structure in the cloud system, which was also observed as a lightning activity. Aggregation and riming were the dominant microphysical processes that contributed to the precipitation. Intense downdraft with high vertical extent (more than 7 km) was observed in the initial convective phase. During the stratiform counterpart, the graupel amount got reduced and significant amount of snow and ice crystal was present, indicating the dominance of

aggregation and vapor deposition processes. Snow became the dominant hydrometeor type during this phase. Considerable reduction in fall velocity, the presence of melting layer, formation of the anvil and genesis of cold-pool were noted during this phase. After the stratiform rain, the system moved towards south-west and residual clouds were noted over the study region without any surface precipitation.

The accumulated rainfall on 12-Sept-2015 (between 00:00 and 18:30 UTC) was 25.50 mm, which was associated with the system (total 25.50 mm rainfall which was observed between 09:48 and 13:34 UTC). The accumulated convective rainfall associated with the system (between 09:48 and 11:00 UTC) was 23.17 mm which accounts for 90.86% of the total rainfall and rainfall from the stratiform counterpart (between 11:00 and 13:34 UTC) was 2.33 mm which accounts for 9.14% of the total rainfall. WRF simulation shows mixed-phase cloud processes played a crucial role in surface precipitation and maximum surface precipitation was associated with the melting of graupel.

Various state of the art instruments and simulation of the WRF model in cloud-resolving scale have enabled us to understand the evolution of the cloud cluster in details over the rain shadow region of WGs. The main conclusions of the study are,

- The confluence of the flow features; westerlies in association with cyclonic circulation over the Arabian Sea, the outflow from Anticyclonic circulation over northwest India and upper-level easterlies from BoB provided large scale conditions favorable for the formation of a convergence zone over the study area.
- There were clear indications for the BL development and subsequent moistening of middle layers through moist penetrative thermals as revealed by a MWRP (temperature and moisture) and WPR observations (updrafts). This lead to sustained CAPE throughout the daytime, prior to the occurrence of the system.
- The study also showed that before the initiation of the system, the FL and WBT$_0$ height had increased, in association with the strong updraft which carried warm moist air to upper layers. This could be identified as the gust front, initiating the cloud

development by lifting a significant amount of moisture to the middle atmosphere.

- A comparison of the observations and numerical simulations showed reasonable spatiotemporal similarity in the events associated with the cloud cluster. On the basis of this, microphysical aspects of the cloud system have been investigated with a detailed analysis of model microphysics.
- Graupel (formed due to riming and drop freezing) and snow (formed due to aggregation) were the main types of hydrometeor, which contributed to maximum mass and precipitation by melting.
- The presence of deep warm cloud layer enhanced the liquid water content at higher altitudes and was trivial for the mixed phase cloud evolution, contributing to sustained lightning activity both during the occurrence of a convective and stratiform part of the cloud cluster.

Being a case study of a convective cloud cluster over the rain shadow region of WGs it possesses its inherent limitation; i.e. the features which have been observed in the present study may not be similar for all the rainfall events over this location. To come up with a robust theory on the dynamical and microphysical processes associated with the rain bearing cloud systems over the rain shadow region of WGs, several such rainfall events have to be analysed in details using variety of observations and numerical simulation.

Appendix

CAPE

Convective available potential energy (CAPE) indicates the maximum amount of energy, associated with an ascending air parcel, available for convection. It is considered as the integrated positive area on a Skew-T sounding and expresses the atmospheric condition between the level of free convection (LFC) and level of neutral buoyancy (LNB). Mathematically it is defined as:

$$CAPE = \int_{LFC}^{LNB} g \frac{T_{v,parcel} - T_{v,env}}{T_{v,env}} dz$$

where $T_{v,\,parcel}$ denotes the virtual temperature of the ascending parcel, $T_{v,env}$ denotes the virtual temperature of the environment and 'g' denotes the gravitational acceleration.

CAPE is measured in Joules per kilogram ($J\ kg^{-1}$). It is a very useful indicator for the formation of the convective system. A higher value of CAPE indicates a high probability of convection with intense updraft speed.

CINE

Convective inhibition (CINE) measures the required amount of energy to overcome the negatively buoyant area of a Skew-T diagram for convection to occur. A triggering mechanism is required to overcome the inhibition. Surface heating, frontal lifting, lower level convergence, and upper-level divergence can act as good triggering mechanism. Mathematically CINE is defined as:

$$CINE = \int_{Sfc}^{LFC} g\,\frac{Tv,parcel - Tv,env}{Tv,env}\,dz$$

where $T_{v,\ parcel}$ denotes the virtual temperature of the ascending parcel, $T_{v,env}$ denotes the virtual temperature of the environment and 'g' denotes the gravitational acceleration.

The unit of CINE is Joules per kilogram ($J\ kg^{-1}$). It measures the stability of the atmosphere. Higher (negative) value of CINE makes an unfavorable condition for convection to occur. Convection is likely to occur with a high CAPE, low CINE in presence of triggering mechanism.

Publisher's Note Springer Nature remains neutral with regard to jurisdictional claims in published maps and institutional affiliations.

REFERENCES

Arnaud, Y., Desbois, M., & Maizi, J. (1992). Automatic tracking and characterization of african convective systems on meteosat pictures. *Journal of Applied Meteorology, 31,* 443–453. https://doi.org/10.1175/1520-0450(1992)031<0443:ATACOA>2.0.CO;2.

Balaji, B., Prabha, T. V., Rao, Y. J., Kiran, T., Dinesh, G., Chakravarty, K., et al. (2017). Potential of collocated radiometer and wind profiler observations for monsoon studies. *Atmospheric Research, 194,* 17–26. https://doi.org/10.1016/j.atmosres.2017.04.023.

Cimini, D., Nelson, M., Güldner, J., & Ware, R. (2015). Forecast indices from a ground-based microwave radiometer for operational meteorology. *Atmospheric Measurement Techniques, 8,* 315–333. https://doi.org/10.5194/amt-8-315-2015.

Dee, D. P., Uppala, S. M., Simmons, A. J., Berrisford, P., Poli, P., Kobayashi, S., et al. (2011). The ERA-Interim reanalysis: Configuration and performance of the data assimilation system. *Quarterly Journal of the Royal Meteorological Society, 137,* 553–597. https://doi.org/10.1002/qj.828.

Dixon, M., & Wiener, G. (1993). TITAN: Thunderstorm identification, tracking, analysis, and nowcasting—a radar-based methodology. *Journal of Atmospheric and Oceanic Technology.* https://doi.org/10.1175/1520-0426(1993)010%3c0785:ttitaa%3e2.0.co;2.

Dudhia, J. (1989). Numerical study of convection observed during the winter monsoon experiment using a mesoscale two-dimensional model. *Journal of the Atmospheric Sciences, 46,* 3077–3107. https://doi.org/10.1175/1520-0469(1989)046%3c3077:NSOCOD%3e2.0.CO;2.

Francis, P. A., & Gadgil, S. (2006). Intense rainfall events over the west coast of India. *Meteorology and Atmospheric Physics, 94,* 27–42. https://doi.org/10.1007/s00703-005-0167-2.

Goyens, C., Lauwaet, D., Schröder, M., Demuzere, M., & Van Lipzig, N. P. M. (2011). Tracking mesoscale convective systems in the Sahel: Relation between cloud parameters and precipitation. *International Journal of Climatology, 32,* 1921–1934. https://doi.org/10.1002/joc.2407.

Gunnell, Y. (1997). Relief and climate in south Asia: The influence of the western ghats on the current climate pattern of peninsular India. *International Journal of Climatology, 17,* 1169–1182. https://doi.org/10.1002/(SICI)1097-0088(199709)17:11<1169::AID-JOC189>3.0.CO;2-W.

Hagos, S., Feng, Z., Burleyson, C. D., Lim, K.-S. S., Long, C. N., Wu, D., et al. (2014). Evaluation of convection-permitting model simulations of cloud populations associated with the Madden-Julian Oscillation using data collected during the AMIE/DYNAMO field campaign. *Journal of Geophysical Research Atmospheres, 119*(21), 12052–12068. https://doi.org/10.1002/2014JD022143.

Hong, S.-Y., Noh, Y., & Dudhia, J. (2006). A new vertical diffusion package with an explicit treatment of entrainment processes. *Monthly Weather Review, 134,* 2318–2341. https://doi.org/10.1175/MWR3199.1.

Huffman, G. J., Stocker, E. F., Bolvin, D. T., Nelkin, E. J., & Jackson T. (2019). GPM IMERG final precipitation L3 half hourly 0.1 degree × 0.1 degree V06, Greenbelt, MD, Goddard Earth Sciences Data and Information Services Center (GES DISC). https://doi.org/10.5067/gpm/imerg/3b-hh/06. Accessed 09 June 2019.

Kain, J. S. (2004). The Kain–Fritsch convective parameterization: An update. *Journal of Applied Meteorology, 43,* 170–181. https://doi.org/10.1175/1520-0450(2004)043%3c0170:TKCPAU%3e2.0.CO;2.

Konwar, M., Das, S. K., Deshpande, S. M., Chakravarty, K., & Goswami, B. N. (2014). Microphysics of clouds and rain over the Western Ghat. *Journal of Geophysical Research Atmospheres, 119,* 6140–6159. https://doi.org/10.1002/2014JD021606.

Lim, K.-S. S., & Hong, S.-Y. (2010). Development of an effective double-moment cloud microphysics scheme with prognostic cloud condensation nuclei (CCN) for weather and climate models. *Monthly Weather Review, 138,* 1587–1612. https://doi.org/10.1175/2009MWR2968.1.

Maheskumar, R. S., Narkhedkar, S. G., Morwal, S. B., Padmaku-mari, B., Kothawale, D. R., Joshi, R. R., et al. (2014). Mechanism of high rainfall over the Indian west coast region during the monsoon season. *Climate Dynamics, 43,* 1513–1529. https://doi.org/10.1007/s00382-013-1972-9.

Mathon, V., & Laurent, H. (2001). Life cycle of Sahelian mesoscale convective cloud systems. *Quarterly Journal of the Royal Meteorological Society, 127,* 377–406. https://doi.org/10.1002/qj.49712757208.

Mathon, V., Laurent, H., & Lebel, T. (2002). Mesoscale convective system rainfall in the Sahel. *Journal of Applied Meteorology, 41,* 1081–1092. https://doi.org/10.1175/1520-0450(2002)041%3c1081:MCSRIT%3e2.0.CO;2.

Min, K. H., Choo, S., Lee, D., & Lee, G. (2015). Evaluation of WRF cloud microphysics schemes using radar observations. *Weather and Forecasting, 30*(6), 1571–1589. https://doi.org/10.1175/WAF-D-14-00095.1.

Mlawer, E. J., Taubman, S. J., Brown, P. D., Iacono, M. J., & Clough, S. A. (1997). Radiative transfer for inhomogeneous atmospheres: RRTM, a validated correlated-k model for the longwave. *Journal of Geophysical Research, 102,* 16663–16682. https://doi.org/10.1029/97JD00237.

Murthy, B. S., Latha, R., & Madhuparna, H. (2018). WRF simulation of a severe hailstorm over Baramati: A study into the space–time evolution. *Meteorology and Atmospheric Physics, 130,* 153–167. https://doi.org/10.1007/s00703-017-0516-y.

Patwardhan, S. K., & Asnani, G. C. (2000). Meso-scale distribution of summer monsoon rainfall near the Western Ghats (INDIA). *International Journal of Climatology, 20,* 575–581. https://doi.org/10.1002/(SICI)1097-0088(200004)20:5<575::AID-JOC509>3.0.CO;2-6.

Prabha, T. V., Goswami, B. N., Murthy, B. S., & Kulkarni, J. R. (2011). Nocturnal low-level jet and 'atmospheric streams' over the rain shadow region of Indian Western Ghats. *Quarterly Journal of the Royal Meteorological Society, 137,* 1273–1287. https://doi.org/10.1002/qj.818.

Rao, Y. P. (1976). *Southwest Monsoon.*

Segele, Z. T., Leslie, L. M., & Lamb, P. J. (2013). Weather research and forecasting model simulations of extended warm-season heavy precipitation episode over the US southern great plains: Data assimilation and microphysics sensitivity experiments. *Tellus Series A Dynamic Meteorology and Oceanography, 65,* 1–28. https://doi.org/10.3402/tellusa.v65i0.19599.

Soman, M. K., & Kumar, K. (1990). Some aspects of daily rainfall distribution over India during the south-west monsoon season. *International Journal of Climatology, 10,* 299–311.

Song, H. J., & Sohn, B. J. (2018). An evaluation of WRF microphysics schemes for simulating the warm-type heavy rain over the Korean Peninsula. *Asia-Pacific Journal of Atmospheric Sciences, 54*(2), 225–236. https://doi.org/10.1007/s13143-018-0006-2.

Tawde, S. A., & Singh, C. (2015). Investigation of orographic features influencing spatial distribution of rainfall over the Western Ghats of India using satellite data. *International Journal of Climatology, 35,* 2280–2293. https://doi.org/10.1002/joc.4146.

Tewari, M., Chen, F., Wang, W., Dudhia, J., LeMone, M. A., Mitchell, K., Ek, M., Gayno, G., Wegiel, J., & Cuenca, R. H. (2004). Implementation and verification of the unified noah land surface model in the WRF model. In *20th conference on weather analysis and forecasting/16th conference on numerical weather prediction, American Meteorological Society, Seattle, WA, US*, pp. 11–15.

Utsav, B., Deshpande, S. M., Das, S. K., & Pandithurai, G. (2017). Statistical characteristics of convective clouds over the western ghats derived from weather radar observations. *Journal of Geophysical Research Atmospheres, 122,* 10050–10076. https://doi.org/10.1002/2016JD026183.

Wu, D., Zhao, K., Kumjian, M. R., Chen, X., Huang, H., Wang, M., Didlake, A. C. Jr., Duan, Y., & Zhang, F. (2018). Kinematics and microphysics of convection in the outer rainband of typhoon nida (2016) revealed by polarimetric radar. *Monthly Weather Review, 146*(7), 2147–2159. https://doi.org/10.1175/MWR-D-17-0320.1.